Bioactive Materials 60 (2026) 74–94

Contents lists available at ScienceDirect

Bioactive Materials

journal homepage: www.keaipublishing.com/en/journals/bioactive-materials

Thermosensitive citrate-based mussel-inspired attack-defense integrated bioadhesives facilitate complicated wound healing

Meimei Fu [a,1], Qiankun Shi [b,1], Yitao Zhao [a,1], Jintao Li [a], Zhuoyi Huang [a,c], Zhihui Lu [a], Jian Yang [d,*], Dongfang Zhou [b,**], Jinshan Guo [a,c,***]

[a] Department of Histology and Embryology, School of Basic Medical Sciences, Guangdong Provincial Key Laboratory of Bone and Joint Degeneration Diseases, The Third Affiliated Hospital of Southern Medical University, Southern Medical University, 1023 Southern Shatai Rd., Guangzhou, 510515, PR China
[b] NMPA Key Laboratory for Research and Evaluation of Drug Metabolism & Guangdong Provincial Key Laboratory of New Drug Screening, School of Pharmaceutical Sciences, Southern Medical University, 1023 Southern Shatai Rd., Guangzhou, 510515, PR China
[c] Suzhou Institute of Biomedical Engineering and Technology, Chinese Academy of Science, Suzhou, 215011, PR China
[d] Research Center for Industries of the Future, Biomedical Engineering Program, School of Engineering, Westlake University, Hangzhou, Zhejiang, 310030, PR China

ARTICLE INFO

Keywords:
Mussel-inspired
Citrate
Thermosensitive
Photothermal therapy (PTT)
Drug-free
Therapeutic tissue adhesive

ABSTRACT

The treatment of complicated wounds remains unsatisfactory due to the lack of a comprehensive strategy synchronously addressing concomitant disease cure along with favorable wound healing. Herein, a family of thermosensitive citrate-based mussel-inspired bioadhesives (TCMBAs) were developed for the first time by mixing poly(ethylene glycol)-block-poly(propylene glycol)-block-poly(ethylene glycol)-incorporated and calcium-containing water-soluble injectable citrate-based mussel-inspired bioadhesive prepolymer with $FeCl_3$ in bicine solution. With a tunable minimum sol-to-gel transition temperature in the range of 28–42 °C, the optimized TCMBAs can be conveniently administrated at room temperature and instantly close wounds at body temperature. TCMBAs exhibit a suite of ideal material properties, including high wet tissue adhesion strength, rapid shape adaptability, self-healing capability, and high elasticity. Furthermore, they demonstrate fast biodegradability, excellent biocompatibility, and potent hemostatic ability. The intrinsic photothermal conversion efficiency of TCMBAs facilitates mild photothermal therapy (PTT), inducing a thermo-mediated cytotoxic effect that effectively eliminates both pathogenic bacteria and cancer cells. This multifunctional "attack–defense" property, combining antimicrobial and antitumor effects with barrier protection and regenerative functions, was demonstrated in infected and cancerous wound models. TCMBA-based treatment under NIR irradiation promoted healing of infected wounds and suppressed tumor recurrence and metastasis while accelerating wound closure. These results highlight TCMBAs as a highly promising platform for the treatment of complex and refractory wounds.

1. Introduction

The clinical demand for effective management of complex wounds, such as post-surgical cancerous wounds after tumor resection, infected wounds, and diabetic chronic wounds, continually increases due to the aging population [1–3]. Effective wound healing requires concomitant disease to be managed. Conversely, non-healing wounds can severely impede the treatment of underlying conditions [1–3]. This is particularly evident in post-surgical cancerous wounds, where residual micro-infiltrations frequently cause tumor recurrence and metastasis, which in turn delays wound healing and may lead to tissue necrosis [4]. Moreover, tumor resection surgery can increase the risk of metastasis.

Peer review under the responsibility of editorial board of Bioactive Materials.
* Corresponding author.
** Corresponding author.
*** Corresponding author. Department of Histology and Embryology, School of Basic Medical Sciences, Guangdong Provincial Key Laboratory of Bone and Joint Degeneration Diseases, The Third Affiliated Hospital of Southern Medical University, Southern Medical University, 1023 Southern Shatai Rd., Guangzhou, 510515, PR China.
E-mail addresses: yangjian07@westlake.edu.cn (J. Yang), dfzhou@smu.edu.cn (D. Zhou), jsguo4127@smu.edu.cn, jsguo4127@163.com (J. Guo).
[1] These authors contribute equally.

https://doi.org/10.1016/j.bioactmat.2026.01.010
Received 3 November 2025; Received in revised form 6 January 2026; Accepted 12 January 2026
Available online 20 January 2026

Wound-associated acute inflammation and the release of damage-associated molecular patterns (DAMPs) trigger systemic immunosuppression [5,6], which, compounded by post-surgical bleeding, promotes local tumor recurrence and distant metastasis [1,7–9]. Unfortunately, conventional closure methods (e.g., sutures, staples) lack bioactive functions and cannot facilitate hemostasis, inhibit tumor recurrence, or promote wound healing [8–10]. Furthermore, they fail to provide an airtight sealing to prevent microbial invasion [11], thus necessitating postoperative systemic antibiotic administration or chemo-/radio-therapy to control infection or prevent tumor recurrence/metastasis [1,7–10,12]. In infected wounds, wound healing and infection control also interact with each other [2]. Therefore, an integrated "attack-defense" strategy that simultaneously eliminates pathological threats (e.g., residual tumor cells, bacteria) and promotes regenerative processes is urgently needed.

As a promising alternative to conventional wound closure devices, tissue adhesives have revolutionized surgical procedures by functioning as sealants and hemostatic agents that provide fluid-impermeable sealing, control bleeding, and promote healing [1,11,13–17]. Although several studies have employed tissue adhesives for infected wound healing or local adjuvant chemo-/immunotherapy [1,3,18], these adhesives were primarily used as drug-loading platforms, akin to hydrogels

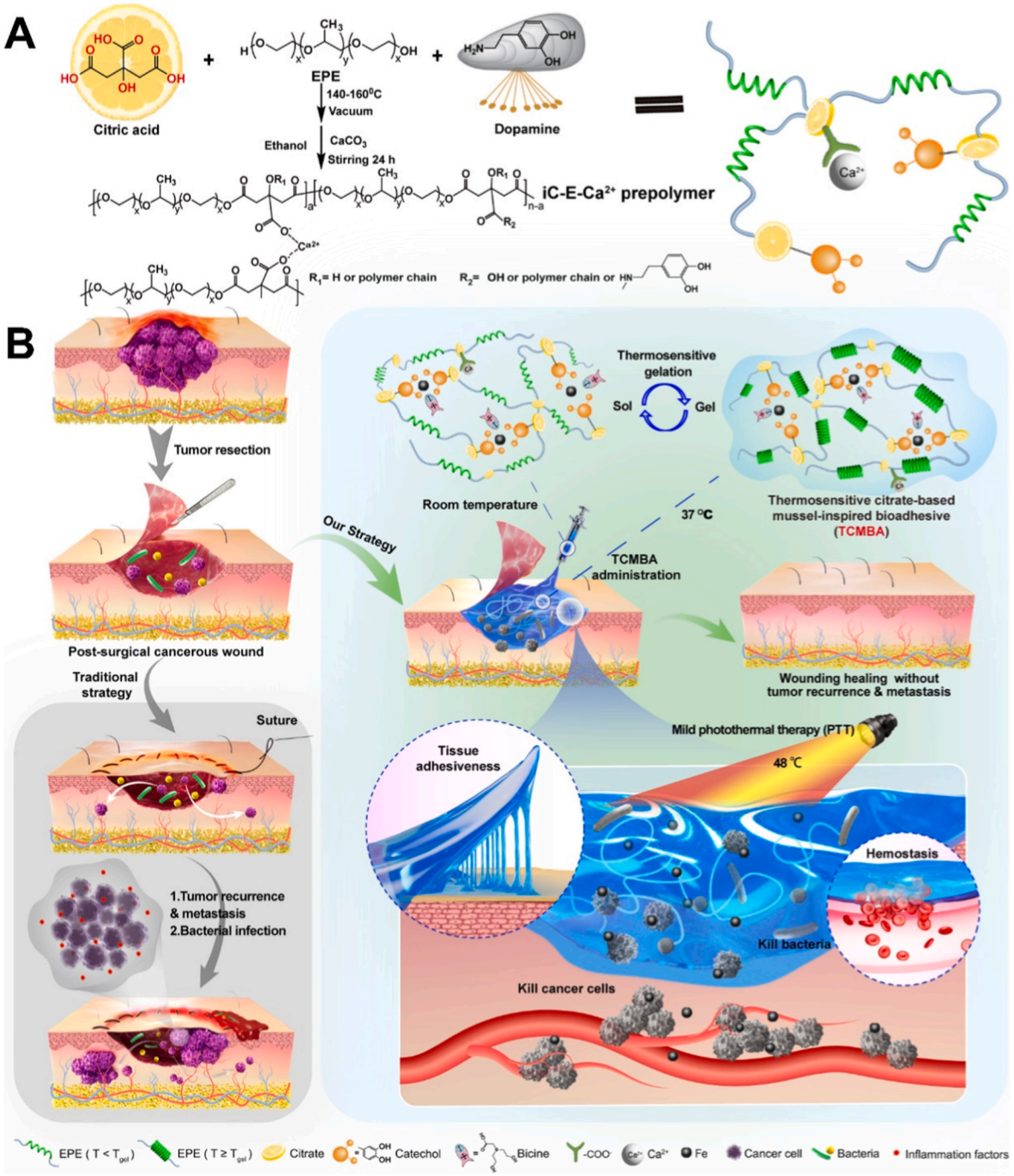

Scheme 1. Schematic illustration of the preparation and working mechanism of TCMBAs. A) Synthesis of calcium-containing water-soluble injectable citrate-based mussel-inspired bioadhesive (iCMBA) prepolymer (iC-E-Ca^{2+}). **B)** Development of thermosensitive citrate-based mussel-inspired bioadhesive (TCMBA) via coordination between iC-E-Ca^{2+} and $FeCl_3$ in bicine solution, and its application for post-surgical wound closure and mild photothermal therapy (PTT) against tumor recurrence, metastasis, and bacterial infection.

[19] or micro-/nano-particles [20–22], and their inherent tissue adhesion and hemostatic capabilities were largely overlooked. Moreover, using tissue adhesives as drug carriers increases complexity, cost, and administrative approval challenges [23]. Therefore, the development of "attack-defense" integrated tissue adhesives that possess inherent therapeutic properties (e.g., antimicrobial, anticancer) without requiring additional drugs represents a highly attractive alternative.

Among various options, mussel-inspired adhesives have attracted intensive research interest due to their robust wet tissue adhesion, which is conferred by covalent bond formation between catechol groups and nucleophilic residues (e.g., amines, thiols) on tissue proteins [13,14,24–29]. Benefiting from the versatile and facile citrate chemistry [30–33], a series of injectable citrate-based mussel-inspired bioadhesives (iCMBAs) has been developed in our group for both soft and hard tissue engineering [17,34–37]. As a key metabolite of the tricarboxylic acid (TCA) cycle, citrate not only promotes normal tissue regeneration via metabonegenic regulation [33] but also exerts anticancer effects. These effects include promoting excessive lipid biosynthesis and cellular senescence in tumor cells [38], suppressing their proliferation, inducing apoptosis, and enhancing their sensitivity to chemotherapeutic agents like cisplatin [39]. Moreover, when polymerized, citrate-based materials have been shown to retain and exert antimicrobial properties, likely due to the local high concentration of citrate units and their disruptive effect on microbial membranes [32–37]. This highlights the potential of citrate-based biomaterials in the regulation of the population and fate of different cell types in post-surgical wounds. Furthermore, upon oxidation under basic conditions or coordination with metal ions, mussel-inspired polymers undergo a transformation into melanin-like polymers that exhibit intrinsic photothermal conversion capabilities [40–42]. Compared to classical photothermal agents (e.g., noble metals, metal sulfides, and toxic organic compounds) [43,44], mussel-inspired agents provide superior biocompatibility, biodegradability, and a reduced risk of long-term organ accumulation. These advantages make them highly promising for photothermal therapy (PTT) in both anticancer and antimicrobial applications.

Herein, through a facile “one-pot” reaction between citric acid (CA), poly(ethylene glycol)-block-poly(propylene glycol)-block-poly(ethylene glycol) (EPE) and dopamine (DP), followed by a reaction with calcium carbonate ($CaCO_3$), a calcium-containing water-soluble iCMBA prepolymer (iC-E-Ca^{2+}) was synthesized (Scheme 1A). By further mixing iC-E-Ca^{2+} solution with $FeCl_3$ in bicine solution, a family of thermosensitive citrate-based mussel-inspired bioadhesives (TCMBAs) was developed (Scheme 1B). TCMBAs can quickly transform from liquid (25 °C) into hydrogel at temperatures ≥28 °C, enabling convenient administration at room temperature and fast wound closure at body temperature. The incorporation of iron-catechol coordination in TCMBAs imparted them with significant cohesion and wet tissue adhesion strengths, fast biodegradability, rapid shape-adaptability, and self-healability. Moreover, TCMBAs exhibited intrinsic photothermal properties, enabling mild photothermal therapy (PTT) effective against both pathogenic bacteria and cancer cells. To demonstrate this attack-defense capability, we thoroughly evaluated the efficacy of TCMBAs *in vitro* and *in vivo*. Studies included treating infected full-thickness skin wounds and post-surgical cancerous wounds (after tumor resection) to assess their ability to prevent recurrence and metastasis while promoting healing.

2. Experimental section

2.1. Materials and general measurements

Citric acid (CA), poly(ethylene glycol)-block-poly(propylene glycol)-block-poly(ethylene glycol) (Pluronic® L-31, PEG-PPG-PEG, EPE, average M_n = 1100 Da), poly(ethylene glycol) (PEG, 200 Da), and calcium carbonate ($CaCO_3$) were purchased from Sigma-Aldrich. Ferric (III) chloride hexahydrate ($FeCl_3{\bullet}6H_2O$) and N, N-di(2-hydroxyethyl) glycine (bicine) were from Meryer Chemical Technology Co., Ltd. (Shanghai, China). Dopamine hydrochloride (DP), sodium hydroxide (NaOH), and hydrochloric acid (HCl) were provided by Aladdin Biochemical Technology Co., Ltd. (China). All chemicals were used without further purification unless otherwise specified. The mouse fibroblasts (L929), breast cancer cell line in BALB/c mice (4T1), *Staphylococcus aureus* (*S. aureus*, ATCC 25923), and *Escherichia coli* (*E. coli*, ATCC 25922) were all purchased from ATCC (Manassas, USA). Cell count kit-8 (CCK-8) used for cell culture was purchased from Dojindo (Tokyo, Japan). LIVE/DEAD® Viability/Cytotoxicity Kit assay was purchased from Beyotime (China). The antibodies used for immunofluorescent and immunohistochemical staining, including rabbit anti-Collagen I antibody (1:100 for IHC/IF, ab270993), rabbit anti-CD31 (CD31: platelet endothelial cell adhesion molecule-1) antibody (1:100 for IHC/IF, ab76533), rabbit anti-TNF-α (TNF-α: tumor necrosis factor-α) antibody (1:100 for IHC/IF, ab215188), anti-CD86 (CD86: cluster of differentiation 86, a marker of M1 macrophage) antibody (1:100 for IHC/IF, ab239075), anti-CD206 (CD206: cluster of differentiation 206, a marker of M2 macrophage) antibody (1:100 for IHC/IF, ab64693), anti-IL-1β (IL-1β: interleukin-1β) antibody (1:100 for IHC/IF, ab315084), and anti-IL-10 (IL-10: interleukin-10) antibody (1:100 for IHC/IF, ab133575) were all from Abcam (Cambridge, UK).

Attenuated total reflectance-Fourier transform infrared (ATR-FTIR) spectra of dried crosslinked polymer adhesive films were recorded by a TENSOR II Brochure-Bruker spectrometer (Germany) with air as background. Scanning electron microscopy (SEM) images were recorded using JSM-IT200 (Japan). The ultraviolet–visible spectroscopy (UV–vis) spectra of prepolymers in DI water were obtained using a UV–vis spectrometer (Shimadzu 2600i, Japan). The rheological properties of the adhesives were evaluated using a TA rheometer (DHR-2, USA).

2.2. Synthesis of iC-E-Ca^{2+} prepolymer

The $CaCO_3$ treated EPE containing injectable citrate-based mussel-inspired bioadhesive (iC-E-Ca^{2+}) prepolymer was synthesized by adapting the method from our previous literature [17,35,45]. Briefly, EPE, CA (1.2 eq. to EPE) and DP (0.25 eq. to EPE) were charged into a 250 mL one-neck round-bottom flask equipped with a magnetic stir bar, and melted at 160 °C under stirring. The melted mixture was then reacted at 140 °C under vacuum and stirred until the stir bar stopped turning at 60 rpm. The obtained crude product was then dissolved in ethanol and reacted with an excess amount of $CaCO_3$ to give a water-soluble iC-E-Ca^{2+} prepolymer with calcium ions on the side carboxyl groups of the prepolymer after dialysis and freeze-drying. The content of catechol group in the iC-E-Ca^{2+} prepolymer was determined to be ~0.200 mmol/g by UV–vis spectrometer.

2.3. Thermosensitive gelation of iC-E-Ca^{2+} with $FeCl_3$ and the minimum sol-to-gel transition temperature (T_{gel}) determination

The citrate-based mussel-inspired bioadhesives were prepared as follows. For each 1 mL aliquot of the iC-E-Ca^{2+} prepolymer solution (30 wt%), a calculated amount of $FeCl_3{\cdot}6H_2O$ (the mole ratio of Fe^{3+} to the catechol groups in iC-E-Ca^{2+}, $R_{Fe/cat}$ = 1/3, 1/6, 1/9, 1/12, 1/15, or 1/18) was dissolved in 0.5 mL of 0.2 M bicine solution. The pH of this solution was then adjusted to 3.0, 5.0, 7.0, 7.5, 8.0, or 8.5, respectively. Then the $FeCl_3$ in 0.2 M bicine solution with different pH values was mixed with 30 wt% iC-E-Ca^{2+} prepolymer solution (V/V = 1/2) to obtain a mixed solution. Interestingly, for most of the formulations tested, the obtained mixed adhesive solutions exhibited a thermosensitive gelation property, thus they were collectively termed thermosensitive citrate-based mussel-inspired bioadhesives (TCMBAs). The thermosensitive adhesive solution stayed in a liquid state at room temperature (25 °C) and formed a hydrogel very quickly at temperatures higher than at least 28 °C. The thermosensitive gelation ability of TCMBAs was demonstrated by injecting the TCMBA solution into water at different temperatures, and the behaviors of the adhesive in water at

different temperatures were photographed. The thermal-crosslinked hydrogel prepared by mixing iC-E-Ca^{2+} prepolymer solution with $FeCl_3$/bicine solution at an $R_{Fe/cat}$ of 1/X was designated as TC-Fe1/X (Table S1, X = 1, 3, 6, 9, 12, 15, or 18). The effect of the $R_{Fe/cat}$ and the pH of the $FeCl_3$/bicine solution on the thermosensitive gelation properties was also investigated.

To determine the sol-to-gel transition temperature (T_{gel}) of all tested formulations, tilting tests in water bath were conducted [34,46]. Specifically, a glass tube containing 1 mL mixed solution was placed in a water bath. The temperature of the water bath was then increased from 20 °C to 60 °C in increments of 1 °C, and held at each target temperature for at least 2 min. At each 1 °C interval, the tube was tilted to observe the flowability of the solution. Gelation was defined as the point at which the solution at the top of the inverted tube remained immobile for >30 s, and the corresponding temperature was recorded as the T_{gel}. Further increasing the temperature led to gel precipitation, and the precipitation temperature was also recorded. For each sample, the tilting tests in water bath were repeated at least three times, and the results were averaged. The effect of prepolymer concentrations and pH values on the T_{gel}s was also investigated.

2.4. Characterizations of prepolymer and adhesives

The UV–vis spectra of iC-E-Ca^{2+} prepolymer with a pH value of 7.4 and of TC-Fe1/9 in 0.2 M bicine solution at pH 6, 8, and 12 were recorded using a UV–vis spectrometer. The ATR-FTIR spectra of the iC-E-Ca^{2+} prepolymer and the dried TC-Fe1/3, TC-Fe1/6, and TC-Fe1/9 adhesives were recorded in the range of 4000–500 cm^{-1}.

2.5. Rheological properties of the adhesives

Before data collection, 400 μL TCMBA solution was placed between two parallel plates (20 mm in diameter) with a gap of 1000 μm at room temperature, and the periphery was sealed by silicone oil to prevent water evaporation. The dynamic viscoelastic properties of the adhesives at 37 °C were characterized by a frequency sweep test (strain = 1%, angular frequency range = 1–100 rad/s). The thermal responsiveness of the adhesives was studied by temperature sweep tests. The temperature was increased from 0 to 60 °C using a heating rate of 2 °C/min. Subsequently, an alternating step strain test was performed at 37 °C and a fixed angular frequency of 10 rad/s to evaluate self-healing behavior [17]. The applied oscillatory strain was alternated between a small amplitude (1%) and a large amplitude (1000%) for four consecutive cycles, with a constant duration of 60 s per strain amplitude.

2.6. Physical properties of TCMBAs

The sol/gel contents of the crosslinked TCMBAs were determined using a solvent extraction method. The adhesive samples were immersed in 1,4-dioxane to dissolve and remove the uncrosslinked (sol) fraction. The remaining insoluble gel fraction was collected, and both fractions were freeze-dried and weighed. The sol contents were then calculated using Equation (1).

$$\text{Sol content}\ (\%) = \frac{W_i - W_d}{W_i} \times 100\ \% \quad (1)$$

Here, W_i represents the initial weight of the dried adhesive, W_d means the dried weight of the adhesive after the sol fraction being removed by solvent.

The swelling ratios of the adhesives were determined as follows. First, the leached and dried samples were weighed to obtain the dry weight (W_d). Each sample was then immersed in deionized water at room temperature for 24 h. Subsequently, the sample was removed, gently blotted with filter paper to remove excess surface water, and immediately weighed to obtain the swollen weight (W_s). The swelling ratio was finally calculated using Equation (2).

$$\text{Swelling ratio}\ (\%) = \frac{W_s - W_d}{W_d} \times 100\ \% \quad (2)$$

The mechanical properties of dried and swollen TCMBA films were measured on a universal material testing machine (Instron 34TM-10, MA, USA) using a 500 N (for dried samples) and 10 N (for swollen samples) load cell according to American Society for Testing and Materials (ASTM) standard D412A. Briefly, rectangle-shaped samples (25 mm × 6 mm × 1.5 mm, length × width × thickness) were pulled to failure under a strain rate of 500 mm/min. The Young's modulus (calculated from the initial slope of the beginning 10% elongation of the curve), tensile strength, and elongation at break were also recorded for different samples. At least five specimens were repeated for each sample, and the results were averaged. To evaluate the effect of pH on the mechanical properties, adhesive samples prepared using $FeCl_3$ solutions at pH 5.0 and 7.5 were tested. In order to evaluate the effect of hydration on the mechanical properties of the adhesives, the mechanical tests were also conducted on samples being hydrated in wet conditions until the weight increased by 10% of the original weight. The results are summarized in Table S2. Additionally, the mechanical compression properties of TCMBA hydrogel were tested at 37 °C over different time points.

The *in vitro* degradation of the TCMBAs was studied by incubating them in phosphate buffered saline (PBS, pH 7.4) at 37 °C. Dry disc specimens (7 mm in diameter, 1 mm thick) were accurately weighed (W_0) and then immersed in tubes containing 10 mL fresh PBS. These tubes were incubated at 37 °C, and the PBS was replaced every other day. At pre-determined time-points, samples were collected, washed with deionized water and freeze-dried. The dry mass was then measured (W_t) and the mass loss percentage was then calculated using Equation (3).

$$\text{Mass loss}\ (\%) = \frac{W_0 - W_t}{W_0} \times 100\ \% \quad (3)$$

The release profile of Fe^{3+} from TCMBA hydrogels was investigated by incubating dried hydrogels of different crosslinking ratios in PBS (0.1 M, pH 7.4) at 37 °C. At predetermined time intervals (0.5, 1, 3, 5, 7, 10, 14, 18, 21, 24, and 28 days), the concentration of Fe^{3+} in PBS solution was quantified using inductively coupled plasma-mass spectrometry (ICP-MS, iCAP PRO, Thermo Fisher Scientific, MA, USA), and the cumulative release percentage was calculated accordingly.

2.7. Rapid shape adaptability and self-healing property of TCMBA

The rapid shape adaptability of TCMBAs was studied using TC-Fe1/9 as the representative. Briefly, certain amounts of TC-Fe1/9 were injected into a star-shaped mold and maintained at 37 °C. The shape change of TC-Fe1/9 was photographed. The TC-Fe1/9 fulfilled the star-shaped mold in less than 15 min.

The self-healing performance of TCMBAs was also studied using TC-Fe1/9 as a representative adhesive. The thermal-crosslinked TC-Fe1/9 was made into a rectangular-shaped sample (25 mm × 6 mm × 1.5 mm, length × width × thickness), and then cut into two parts, which were put together again to observe the self-healing performance. Photographs of the adhesive pieces before and after self-healing were taken. The morphology of the self-healed sites of the test sample was further observed using scanning electron microscopy (SEM).

2.8. Adhesion property of TCMBAs

The universal adhesion of wet TCMBAs to different substrates, including plastic (polystyrene tube, 1.73 g), glass (14.1 g), and metal (200 g), was demonstrated by applying 0.5 mL TC-Fe1/9 (adhered on a plastic glove) onto the surfaces of different substrates, and lifted for at least 30 s. Furthermore, the wet TC-Fe1/9 adhesive was also applied to an operator's knuckle and wrist joints to assess the tissue adhesiveness and the elasticity of the adhesive during skin and joint motion [46].

The adhesion strengths of TCMBAs to wet tissues were measured using porcine skin tissues as the substrate following the Pharmaceutical Industry Standard of the People's Republic of China YY/T0729.3–2009, which was adapted from the ASTM standard F2255-05. Briefly, after being treated with fat removal and hair shaving, followed by washing with saline, the fat-free porcine skin was stored in PBS before use. The fat-free porcine skin tissue was cut into rectangular slices with a size of 10 mm × 30 mm (width × length), and 12 μL TCMBA was applied onto the inner surface. Another porcine skin slice was placed on top of the adhesive with an overlapped area of 10 mm × 10 mm at room temperature. The overlapped porcine skin tissue slices were placed at 37 °C under a humidity of ~50% for 2 h to ensure full crosslinking. The fibrin glue, prepared using 10 μL fibrinogen solution (Sigma-Aldrich) and 2 μL thrombin solution (Sigma-Aldrich) per the manufacturer's manual, was used as the control. The lap shear strength test was conducted on an Instron 34TM-10 machine equipped with a 10 N load cell using a crosshead speed of 5 mm/min under 37 °C. All measurements were repeated at least 5 times for each sample, and the results were averaged.

2.9. Photothermal properties of TCMBAs

The TC-Fe1/9 adhesive disks in 96-well plates (200 μL/well) were irradiated by an 808 nm near-infrared (NIR) laser (MDL-III-808nm-1000 mW, Changchun New Industries Optoelectronics Tech Co., Ltd.) at different power densities (0.25, 0.36, 0.50, 0.64, and 0.75 W/cm^2). The light-induced temperature changes during a 10-min irradiation were monitored with a UTI165H infrared thermal imaging camera. The TC-Fe1/9 adhesive disks were also irradiated with NIR light for four repeated cycles with 5-min irradiation ON and 10-min irradiation OFF for each cycle. The heat maps and temperature change profiles of TCMBAs (TC-Fe1/3, TC-Fe1/6, TC-Fe1/9, TC-Fe1/12) were also recorded using an infrared (IR) thermal camera under a NIR irradiation of 0.50 W/cm^2. The iC-P-Ca^{2+} prepolymer and iC-8 %PI (8 wt% sodium periodate (PI) solution in 0.2 M bicine + 30 wt% iC-P-Ca^{2+} prepolymer solution (V/V = 1/2)) were used as controls. The temperatures were read every 30 s.

To evaluate the effect of NIR irradiation on the adhesion property of TCMBAs, TC-Fe1/9 was applied onto the surface of a transparent glass slice (width × length = 15 mm × 80 mm), and another glass slice was placed on top of the adhesive with an overlapped area of 15 mm × 30 mm. Then the overlapped glass slices were placed at 37 °C under a humidity of ~50% along with a NIR irradiation of 0.50 W/cm^2 for 10 min. The adhesion strengths of TC-Fe1/9 to glass before and after NIR irradiation were measured using the lap shear strength test method mentioned above. The photographs of the TC-Fe1/9 adhered glass slices before and after NIR irradiation were also taken for observation. The effect of NIR irradiation on the wet tissue adhesion strength was also studied using porcine skin through a similar process.

The photo-responsiveness of TCMBAs upon NIR irradiation was also assessed using TC-Fe1/9 as the representative. The wet TC-Fe1/9 adhesive films were irradiated with 808 nm NIR light (0.50 W/cm^2). During irradiation, the temperature changes were recorded. Simultaneously, changes in transmittance and morphology were photographed.

The *in vivo* photothermal properties of TCMBAs were also studied using BALB/c nude mice (female, 15–18 g, 4–6 weeks old). Briefly, the mice were anesthetized with 10 wt% chloral hydrate and 1 % lidocaine, then a certain amount of TC-Fe1/9 was injected subcutaneously into the back and irradiated with NIR laser (0.50 W/cm^2), and the temperature change was recorded. Untreated nude mice and the mice injected with fibrin glue were used as controls. At the same injection site, the thermal changes of the TC-Fe1/9 injected mice after 1, 3, 5 and 7 days were also recorded by a UTI165H infrared thermal imaging camera.

2.10. In vitro NIR photothermal antibacterial properties of TCMBAs

The photothermal antibacterial properties of TCMBAs were assessed using *S. aureus* and *E. coli* as representative Gram-positive and Gram-negative bacteria, respectively. *S. aureus* and *E. coli* were cultured at 37 °C in sterilized Luria-Bertani (LB) broth with a shaking speed of 150 rpm in a rotary shaker overnight, and the obtained bacterial suspensions were diluted before use.

The antibacterial performance of TCMBAs (TC-Fe1/3, TC-Fe1/6, TC-Fe1/9, and TC-Fe1/12) was evaluated by direct exposure to bacterial suspensions. Poly(ethylene glycol) diacrylate (PEGDA)/2-hydroxyethyl methacrylate (HEMA) hydrogel prepared according to our previous literature [34] was used as a negative control. Briefly, the dried TCMBA disks (15 mm in diameter, 1 mm thick) were placed into the wells of 24-well plates followed by the addition of 1 mL bacteria suspension (~1 × 10^6 colony forming units (CFUs)/mL) in each well. Then the samples were exposed to NIR irradiation (808 nm, 0.5 W/cm^2) for 10 min, and the treated bacteria were cultured at 37 °C for 24 h before measuring the optical density (OD) values of the bacteria suspensions at 600 nm. The samples containing TCMBA or PEGDA/HEMA hydrogels but without NIR irradiation, and the blank sample without any treatment, were also set. The bacterial inhibition ratios were calculated using equation (4).

$$\text{Bacterial inhibition ratio}(\%) = 100 - 100 \times \frac{A - A_0}{A_b - A_0} \quad (4)$$

Here, A_0 is the initial OD value of the bacterial suspension, A and A_b are the OD values after 24 h' culture of the sample and blank, respectively.

The inhibitory effect of TCMBA on *S. aureus* biofilm was evaluated using a Transwell assay system, with morphological observation conducted via crystal violet staining. Specifically, an *S. aureus* suspension was inoculated into 24-well plates and cultured for 48 h to allow mature biofilm formation. Then, TCMBAs hydrogel was loaded into the Transwell insert, which was placed above the pre-formed biofilm-containing wells. One experimental group was subjected to NIR irradiation (808 nm, 0.50 W/cm^2) for 10 min, while another group received no irradiation and served as the control. After treatment, the bacteria and the Transwell system were co-cultured for an additional 24 h. Finally, the biofilm was stained with crystal violet, and its area was quantitatively analyzed using ImageJ software.

In addition, 1 mL bacterial suspension was mixed with an equal volume of either citric acid solution (33.0 mg/mL), ferric chloride solution (1.1 mg/mL), iC-E-Ca^{2+} solution (200.0 mg/mL), a homogenized suspension of TC-Fe1/9 hydrogel (equivalent to 1.0 g of the original hydrogel per mL), or the same homogenized TC-Fe1/9 hydrogel suspension subjected to photothermal treatment. An untreated control group of bacterial suspension was also established, along with a 48 °C + 10 min group where the suspension was treated at 48 °C for 10 min. After 12 h of incubation, the absorbance at 600 nm was measured, and diluted spread plating was also performed to evaluate the antibacterial performance of the different components and treatment methods [47].

2.11. In vitro photothermal killing effect of TCMBAs on tumor cells

The photothermal killing effect of TCMBAs on 4T1 cells was assessed using a transwell setup and stained with Live/Dead assay, followed by observing under a fluorescence microscope [48]. First, the 4T1 cells were seeded in the wells of a 24-well plate. After 12 h, the iC-E-Ca^{2+} prepolymer or TC-Fe1/9 hydrogel was added into the transwells and placed on top of the wells of 24-well plates, and treated with NIR irradiation (808 nm, 0.50 W/cm^2) for 10 min. Then the treated cells were cultured for another 4 h at 37 °C and 5% CO_2 before the addition of calcein-AM and propidium iodide (PI), and incubating for an additional 30 min in the incubator. Finally, the Live/Dead stained cells were observed under an inverted fluorescence microscope (Leica DMI4000 B; Leica Microsystems GmbH, Wetzlar, Germany).

2.12. Cytocompatibility of iC-E-Ca^{2+} prepolymer and TCMBAs

The *in vitro* cytocompatibility of TCMBA hydrogels against L929 cells was assessed by studying the cell cytotoxicity of the sol contents (or leachable fractions) and degradation products of the crosslinked hydrogels, according to the processes described in our previous literature [17,35,45]. The sol content solutions of the hydrogels were obtained by incubating 1.0 g dried hydrogel specimens in 10 mL sterile PBS (pH 7.4) for 24 h at 37 °C, followed by removing the floating hydrogels and sterilizing the solutions with 0.2 μm filters to give 1 × solutions. Next, 10 × and 100 × (10 times and 100 times diluted from 1 × solution with PBS) dilutions were prepared. For the cytotoxicity study of sol contents, to each well of a 96-well cell culture plate, 200 μL L929 cell suspension in complete DMEM medium with a density of 5×10^4 cells/mL was added and incubated for 24 h (37 °C, 5% CO_2). Then the sol contents with different dilutions were added to the 96-well plates (20 μL/well) and incubated for another 24 h. Finally, 20 μL CCK-8 solution was added to each well and allowed to incubate for another 1 h before measuring the absorbances at 450 nm with an Epoch™ microplate spectrophotometer (BioTek, USA). The cytotoxicity of the crosslinked hydrogels' degradation products was also evaluated. Briefly, 1.0 g dried TCMBA hydrogel sample or poly (lactic-co-glycolic acid) (PLGA, used as control, LA/GA = 50/50, Mw ~ 30 kDa, purchased from Guangzhou Boqiang Biotechnology Ltd.) was completely degraded in 10 mL 0.2 M NaOH solution. After sterilizing the solutions with 0.2 μm filters and adjusting the pH to 7.4, 1 × degradation solutions were obtained. The 1 × solutions were further diluted into 10 × and 100 × solutions using PBS (pH 7.4). These dilutions of the degradation products were then tested for cytotoxicity using the same cell culture and CCK-8 assay protocol as described for the sol contents.

The viability of cells that were exposed to TCMBA hydrogels was evaluated using the Live/Dead Viability/Cytotoxicity Kit assay (Beyotime, China). After 6 h of co-incubation, the cells were stained according to the manufacturer's instructions (Beyotime, China) and visualized using an inverted fluorescence microscope (Leica DMI4000 B).

2.13. In vivo hemostatic capacity and hemocompatibility of TCMBAs

The hemostatic performance of TCMBAs (using TC-Fe1/9 as the representative) was assessed using a Sprague-Dawley (SD) rat tail amputation model. All *in vivo* experiments were performed with the approval of the Animal Experimental Committee of Institute of Biological and Medical Engineering, Guangdong Academy of Sciences (Approval No. 2021011). Briefly, the tails of rats were transected with a sterile razor blade at the site 2 cm from the base of the rat's tail. 200 μL of TC-Fe1/9 or fibrin glue was immediately applied to the bleeding site. An untreated group was also set as a blank control. The bleeding time was defined as the time from the start of transection to bleeding cessation. Both the amounts of bleeding and hemostatic times were recorded. All measurements were repeated at least 3 times, and the results were averaged.

To evaluate the hemocompatibility of TCMBAs, an *in vitro* hemolysis assay was conducted. The experiment was divided into four groups: negative control (PBS), positive control (0.1% Triton X-100), fibrin glue group, and TC-Fe1/9 material group. Each material was co-incubated with fresh anticoagulated whole blood at 37 °C for 1 h. After incubation, the samples were centrifuged, and the supernatant was collected to measure its absorbance at 540 nm, from which the hemolysis rate was calculated.

2.14. In vivo infection wound healing performance of TCMBAs

The infection wound healing property of TCMBAs was evaluated by a full-thickness skin arc-incision model on mice adapted from previous literature [17,49]. All *in vivo* experiments were performed with the approval of the Animal Experimental Committee of Institute of Biological and Medical Engineering, Guangdong Academy of Sciences (Approval No. 2021011). Briefly, 50 BALB/c nude mice (15–18 g, 4–6 week old, female) were randomly divided into five groups and anesthetized with 10 wt% chloral hydrate and 1% lidocaine in local, then fixed on a surgical corkboard. After shaving and sterilizing with iodine, a full-thickness arc-incision (2 cm length) was created on the side of the abdomen of the mice. Then, *S. aureus* (50 μL, ~1×10^6 CFU/mL) was added to the incision to create the infected incision model. TC-Fe1/9 was selected as the representative of TCMBAs to treat the infected incision with and without NIR irradiation (808 nm, 0.5 W/cm^2, 10 min). The infected incisions treated with suture or Fibrin glue (consisting of fibrinogen and prothrombin) were set as negative controls. Meanwhile, an uninfected group was also set as a positive control. On the 3rd day, some mice were sacrificed, and the infected tissues were harvested, washed to collect the living microbes and conduct bacteria colony-counting experiments according to the processes described in previous literature [49]. Additionally, on the 3rd, 7th, and 14th day, the treated incisions were photographed and the incision lengths were measured by ImageJ. On the 7th and 14th day, the treated incision tissues were sectioned into 4 μm-thick slices and studied with hematoxylin and eosin (H&E) and Masson trichrome staining. The collagen density (%) was determined by calculating the ratio of blue-stained area to the total area of Masson trichrome staining images using ImageJ. At least 5 random areas were selected, and the results were averaged. To further evaluate tissue healing, the collagen type IA1 (COL1A1) and platelet endothelial cell adhesion molecule-1 (CD31) immunofluorescent staining were also conducted, and the relative expression levels of COL1A1 and CD31 positive cells for different groups were also calculated using ImageJ. Moreover, on the 7th and 14th day, the healed skins were cut into 5 mm × 30 mm rectangular slices, and their tensile mechanical properties were studied with a tensile test until failure on an Instron Materials Test system (Instron, 34TM-10) equipped with a 500 N load cell with a cross-head speed of 5 mm/min under ambient condition.

2.15. In vivo photothermal therapy (PTT) to prevent tumor recurrence

First, the tumor-bearing mice model was established by subcutaneously injecting 1×10^7 4T1 cancer cells in 100 μL PBS into the left rear flank of the Balb/c nude mice (6 weeks old, female, 30 ± 5 g), and the tumor volumes were allowed to reach 50–60 mm^3. All the animal experiments were conducted with the approval of Animal Experimental Committee of Institute of Biological and Medical Engineering, Guangdong Academy of Sciences (Approval No. 2021011). 25 mice were randomly divided into five groups: (1) mice undergoing tumor removal surgery only, (2) mice undergoing tumor removal surgery and treated with fibrin glue, (3) mice undergoing tumor removal surgery and treated with fibrin glue + NIR, (4) mice undergoing tumor removal surgery and treated with TC-Fe1/9, (5) mice undergoing tumor removal surgery and treated with TC-Fe1/9+NIR. The tumor-bearing mice were anesthetized by isoflurane, then a skin incision was created at the edge of the tumor, and the main tumor body was surgically excised along the boundary between tumor and normal tissues. The resulting surgical wounds were either sutured with commercially available sutures (the suture group) or closed with Fibrin glue/TCMBA (using TC-Fe1/9). For the mice undergoing additional postoperative PTT treatment, the anesthetized mouse was fixed on the surgical board, and the entire wound region was covered by TC-Fe1/9 and irradiated with the 808 nm laser (0.5 W/cm^2, 10 min). The tumor sizes of the treated mice were measured by a caliper every 3 days. The mice weights and the tumor-free rates were also measured and calculated. On the 14th and 21st days, the treated incisions were also photographed, and the incision lengths were also measured using ImageJ.

The apoptotic response in tumor tissues was evaluated by terminal deoxynucleotidyl transferase-mediated dUTP-digoxigenin nick-end labeling (Tunel) staining. The major organs (including heart, liver, spleen, lungs, and kidneys) were also harvested and studied by H&E staining to

evaluate the anti-recurrence efficacy and systemic toxicity of TC-Fe1/9+NIR. The presence and number of lung nodules on the lung surface and within the parenchyma were quantified through H&E staining to assess whether tumor lung metastasis occurred or not in each group. To assess the wound healing and anti-tumor performance, the skin and tumor tissue slices harvested after 21 days were also studied by histological (H&E), immunofluorescent (tumor necrosis factor α (TNF-α), CD31, CD86, and CD206), and immunohistochemical (IL-1β and IL-10) staining. In the immunofluorescent staining, FITC-conjugated goat anti-rabbit IgG (CST, USA) was used as the secondary antibody to reveal relative protein expression, and the nuclei were stained with DAPI (4′, 6-diamidino-2-phenylindole, Beyotime, China) containing mounting solution. Additionally, macrophages were isolated from the tumor resection sites tissue using enzymatic digestion. These macrophages were stained with PE-labeled CD206 antibody and APC-labeled CD86 antibody to distinguish M2 and M1 macrophages, respectively. Flow cytometry was employed to detect and analyze macrophage subpopulations in each sample group.

2.16. Statistical analysis

All quantitative results were statistically analyzed by GraphPad Prism 9 (GraphPad Software, USA) and expressed as mean ± standard deviation. The statistical difference was determined by *t*-test or one-way

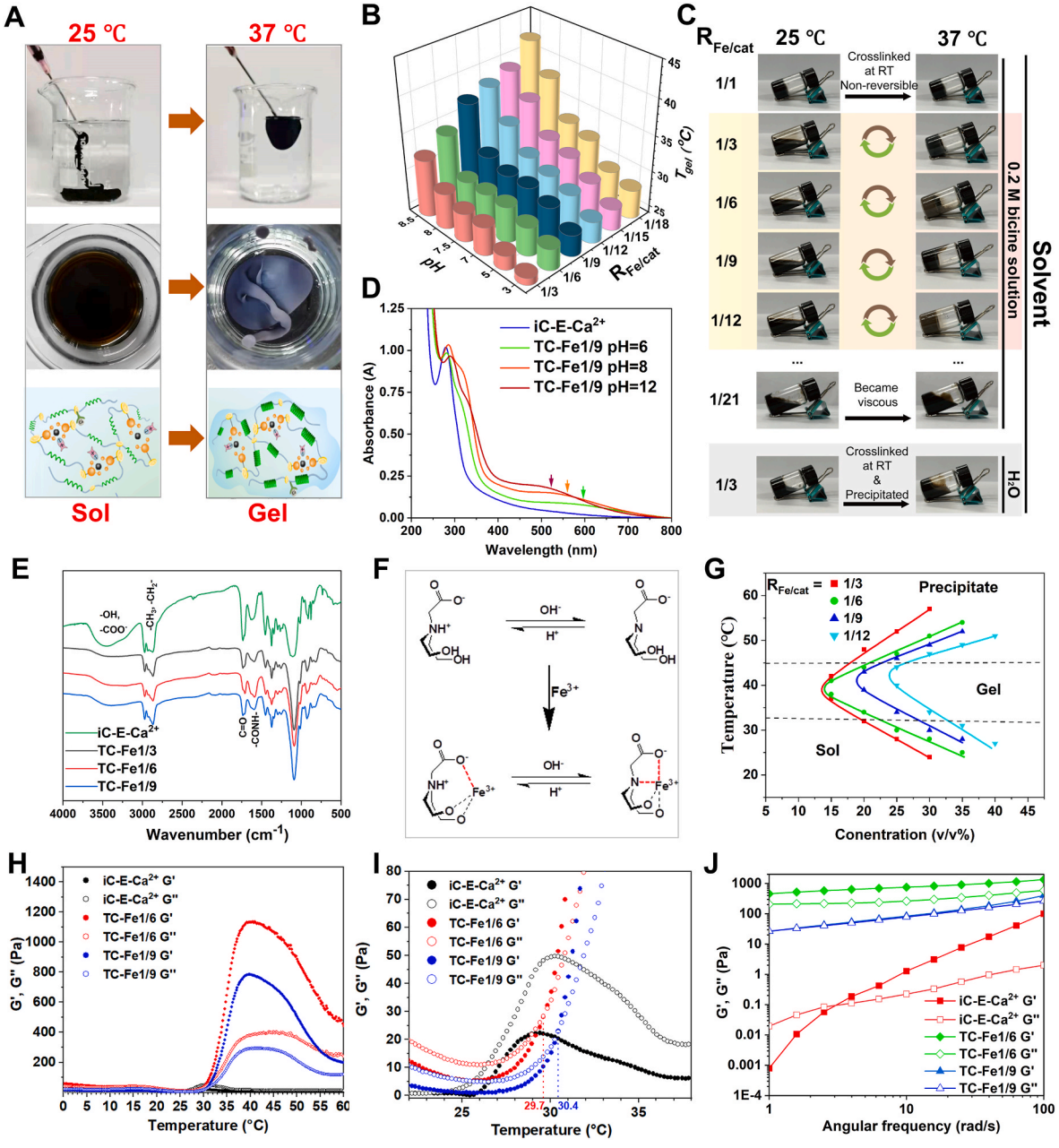

Fig. 1. Characterization and thermosensitive gelation of TCMBA bioadhesives. A) Photographs of the reversible thermosensitive sol-to-gel transition of TCMBA. **B)** The effect of the Fe^{3+}/catechol molar ratio ($R_{Fe/cat}$) and the pH value of $FeCl_3$ in bicine solution on the minimum sol-to-gel transition temperature (T_{gel}) of TCMBA (iC-E-Ca^{2+} concentration = 30 wt%). **C)** Gelation process and temperature-dependent behavior of iC-E-Ca^{2+}/$FeCl_3$ mixtures with different RFe/cat in water or bicine solution. **D)** UV–vis spectra of iC-E-Ca^{2+} and TC-Fe1/9 at pH 6, 8, and 12. **E)** FTIR spectra of the representative crosslinked TCMBA films. **F)** Proposed chelation modes between bicine and Fe^{3+} under acidic and basic conditions. **G)** Phase diagram of TCMBAs when the pH value of $FeCl_3$ in bicine solution = 7.5. **H)** Representative temperature-sweep rheological profiles of TCMBAs and iC-E-Ca^{2+} solutions. **I)** Magnified view of the sol-to-gel transition region from (H). **J)** Frequency-dependent oscillatory rheological behavior of TCMBA and the iC-E-Ca^{2+} precursor solution at 37 °C.

ANOVA. The differences were taken to be significant if $p < 0.05$ (*) was obtained. *, ** and *** represent $p < 0.05$, $p < 0.01$ and $p < 0.001$, respectively.

3. Results and discussion

3.1. Development and characterization of TCMBAs

3.1.1. Synthesis of iC-E-Ca^{2+} Prepolymer

To introduce the hydrophobic EPE (Pluronic® L-31, 1100 Da, cloud point = 37 °C) into iCMBA and make the prepolymer water-soluble, after the polycondensation reaction between CA, EPE, and DP to give iC-E prepolymer, the side carboxyl groups were further reacted with $CaCO_3$ and converted into calcium salt (iC-E-Ca^{2+}) [17,35]. The availability of reactive catechol hydroxyl groups in iC-E-Ca^{2+} prepolymer was confirmed by the presence of the UV absorption peak at approximately 280 nm (Fig. S1). Additionally, the successful incorporation of dopamine was further evidenced by the appearance of the characteristic peaks of the amide group (-C(=O)–NH-) at 1620 cm^{-1} and the benzene ring of the catechol group at 735 cm^{-1} in the FTIR spectrum of iC-E-Ca^{2+} prepolymer (Fig. S2) [35,50].

3.1.2. Thermosensitive gelation of TCMBAs

The mixed solution of iC-E-Ca^{2+} with $FeCl_3$ (in 0.2 M bicine solution) was found to quickly transition from liquid at room temperature (25 °C) to a hydrogel state at 37 °C within 3–46s. This hydrogel could revert to a liquid state when the temperature was reduced to 25 °C (Fig. 1A, Table S1, Movie S1 and S2), demonstrating favorable thermosensitive gelation capability. When the concentration of iC-E-Ca^{2+} prepolymer solution was maintained at 30 wt%, the effect of the pH value of $FeCl_3$ in bicine solution and the molar ratio of Fe^{3+}/catechol ($R_{Fe/cat}$) on the minimum sol-to-gel transition temperatures (T_{gel}s) is shown in Fig. 1B. Lower $R_{Fe/cat}$ ratios resulted in higher T_{gel}s, with $T_{gel} \leq 25$ °C observed when $R_{Fe/cat} \geq 1/3$. Furthermore, the gelation behavior was studied at different temperatures (room temperature or 37 °C) using varying ratios of iC-E-Ca^{2+} to $FeCl_3$ in either 0.2 M bicine solution or aqueous medium (Fig. 1C). No thermosensitive gelation was observed for $R_{Fe/cat} \geq 1/1$ and $R_{Fe/cat} \leq 1/21$. Although Pluronic® F-127 (also named as Poloxamer 407), a representative poly(ethylene glycol)-block-poly(propylene glycol)-block-poly(ethylene glycol) copolymer with a molecular weight of 12.6 kDa, is a well-known thermosensitive material [51], the macromolecular monomer, poly(ethylene glycol)-block-poly(propylene glycol)-block-poly(ethylene glycol) (Pluronic® L-31, EPE, average Mn = 1100 Da), used in the synthesis of iC-E-Ca^{2+} also has a cloud point at 37 °C (1 wt% aqueous solution). EPE itself cannot transform into a hydrogel at 37 °C, nor can its copolymer with citrate and dopamine, iC-E-Ca^{2+}. Consistently, pure iC-E-Ca^{2+} solution, even at a high concentration of 50 wt%, did not gel in the temperature range of 25–50 °C (Fig. S3), highlighting the importance of iron-catechol coordination in the thermosensitive gelation of TCMBAs [44]. The introduction of Fe^{3+} and adjustment of pH to 8.0 resulted in the appearance of a new absorption peak at 575 nm, which might be assigned to the catechol-Fe^{3+}coordination. However, no absorption in the range of 400–600 nm was observed for the prepolymer solution, and the absorption under acidic condition was also relatively weaker than that at basic conditions (Fig. 1D). The formation of iron-catechol coordination and –COO—Fe^{3+}—OOC– ionic bonds was also reflected by the observed peak shrinkage and shift of –COOH and phenolic hydroxyl groups at ~3500 cm^{-1} (Fig. S2) to ~3550 cm^{-1} after crosslinking with $FeCl_3$ (Fig. 1E). Furthermore, T_{gel} increased with the increase of pH, which might be attributed to the pH-responsive chelation between the zwitterion in bicine and Fe^{3+} (Fig. 1F). At basic condition (pK_a of bicine = 8.3), the amine group in bicine was deprotonated, and a stable iron-bicine complex formed, which greatly reduced the chance of iron-catechol coordination, resulting in elevated T_{gel}s. Therefore, at pH ≤ 7.5, the effect of $R_{Fe/cat}$ on T_{gel} was not significant, and T_{gel}s remained within a narrow range of 25–33 °C. However, at pH = 8.0 or 8.5, as $R_{Fe/cat}$ decreased, T_{gel}s significantly increased from 29 or 32 °C ($R_{Fe/cat}$ = 1/3) to 38 or 42 °C ($R_{Fe/cat}$ = 1/18), respectively (Fig. 1B). The effect of iC-E-Ca^{2+} prepolymer concentration on the T_{gel} of TCMBA and the sol-gel-precipitate phase change profiles was further investigated when the pH of $FeCl_3$ solution was kept at 7.5. As shown in the phase diagram (Fig. 1G), all tested iC-E-Ca^{2+}/$FeCl_3$ mixed solutions underwent a sol-gel-precipitate phase transition along with increasing temperature. The gelation temperature windows became narrower and the minimal gelable concentration of iC-E-Ca^{2+} also increased as $R_{Fe/cat}$ decreased from 1/3 to 1/12. The gelation temperature for the tested formulations, especially the ones with a prepolymer concentration of 30 wt% and a pH of $FeCl_3$ solution at 7.5, were in the range of 25–57 °C. The temperature sweep rheology test results shown in Fig. 1H and I also confirm that the T_{gel}s of TC-Fe1/6 and TC-Fe1/9 were ~29.7 and 30.4 °C, respectively, consistent with the tilting test results shown in Fig. 1G. For pure iC-E--Ca^{2+} prepolymer solution, it became sticky at 26 °C, but the loss moduli (G″) were all higher than the storage moduli (G′) in the whole range of 0–60 °C, further confirming that the pure prepolymer solution has no thermosensitive gelation property. After gelation, both the G′ and G″ of crosslinked TCMBAs increased by at least one order of magnitude compared to that of the prepolymer solution (Fig. 1J), in accordance with the temperature sweep rheology test results (Fig. 1H).

In summary, by optimizing the Fe^{3+}/catechol ratio, pH value, and prepolymer concentration, the TCMBA hydrogels with rapid thermosensitive gelation, excellent injectability, and significantly enhanced mechanical properties were successfully prepared. The interesting thermosensitive gelation behavior is believed to rely on the combination of the thermosensitive behavior of EPE as well as the coordination bonds between Fe^{3+} and catechol groups. Concurrently, ionic interactions and chelation between Fe^{3+} and the carboxylate ($–COO^-$) and amine/hydroxyl groups of bicine act as pH-sensitive regulators for Fe^{3+} cross-linking sites, also providing a conditional blocking mechanism for cross-linking.

3.1.3. Physical, mechanical, self-healing, shape adaptability, and tissue adhesion Properties of TCMBAs

The TCMBA formulations (TC-Fe1/3, TC-Fe1/6, TC-Fe1/9, and TC-Fe1/12) crosslinked with $FeCl_3$ in bicine solution (pH 7.5) exhibited a sol content of less than 20 % and a swelling ratio ranging from 200 % to 1000% (Fig. 2A and B). It is noteworthy that as the $R_{Fe/cat}$ value decreased, the sol content gradually increased, accompanied by a significant enhancement in the swelling ratio. This trend provides direct evidence for the iron-mediated iC-E-Ca^{2+} coordination cross-linking structure within the TCMBAs system: a reduction in Fe^{3+} concentration led to a decrease in the density of coordination cross-linking points, resulting in a lower cross-linking density of the hydrogel and the formation of a more porous three-dimensional network structure. This structural characteristic contributes to an improved water absorption capacity, enabling efficient uptake of wound exudate and facilitating optimal moisture management at the wound site. In addition, the tensile strength ranged from 1202.5 ± 136.0 to 1527.5 ± 134.8 kPa, Young's modulus from 1110.5 ± 78.0 to 2273.3 ± 415.5 kPa, and the elongation at break from 809.7% to 1830.4% of these four groups (Fig. 2C and D). A decrease in the Fe^{3+}/catechol molar ratio ($R_{Fe/cat}$) resulted in reduced tensile strength and Young's modulus, along with an increased fracture elongation, indicating a lower cross-linking density. These mechanical behaviors further corroborate the trend observed in sol content and swelling experiments, confirming that a reduction in $R_{Fe/cat}$ leads to a decrease in cross-linking density. The observed decrease in cross-linking density was further manifested in the degradation behavior of TCMBAs and the corresponding iron ion release behavior (Fig. 2E and S4). All tested formulations displayed rapid degradation profiles, with complete mass loss occurring within approximately one week to one month. The release behavior of Fe^{3+} largely correlated with the degradation kinetics across the different formulations. Among the four tested TCMBA

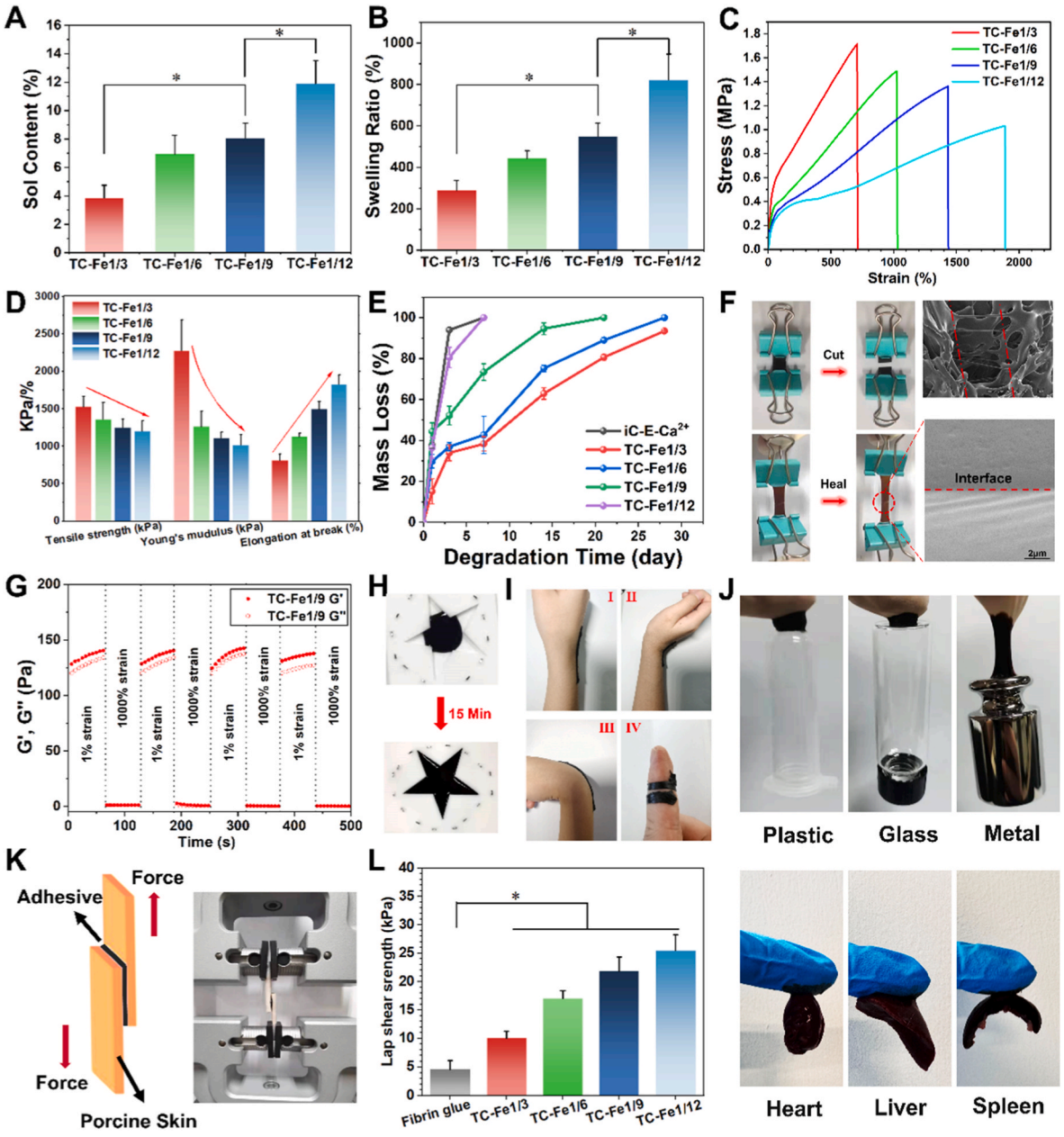

Fig. 2. Comprehensive characterization of TCMBA bioadhesives. A) Sol content, and **B)** swelling ratio of representative TCMBA formulations (n = 5). **C)** Representative tensile stress-strain curves of dried TCMBA films (crosslinked at pH 7.5). **D)** Summary of mechanical properties derived from (C): tensile strength, Young's modulus, and elongation at break (n = 5). **E)** Degradation profiles of representative TCMBA formulations (n = 5). **F)** Macroscopic demonstration of the self-healing process in TC-Fe1/9: two separated gel pieces fused into a single entity capable of being stretched. **G)** Step-strain rheological recovery tests of TC-Fe1/9 (alternating between 1% and 1000% strain) demonstrating its self-healing capability. **H)** Shape-adaptive behavior of TC-Fe1/9, conforming to irregular surfaces. **I)** Demonstrations of robust adhesion between TCMBA and human skin under various mechanical challenges: tensile, compressive, and torsional forces. **J)** Adhesion strength of TCMBAs to various substrates. **K)** Schematic illustration of the lap-shear test setup for evaluating adhesion strength to porcine skin. **L)** Quantitative lap-shear adhesion strengths of various TCMBA formulations to wet porcine skin (n = 5). $^{*}p < 0.05$, $^{**}p < 0.01$, $^{***}p < 0.001$.

formulations, TC-Fe1/3, with the highest iron content, demonstrated the slowest degradation and Fe^{3+} release, extending up to 28 days. In contrast, TC-Fe1/12, with the lowest iron content, showed the most rapid degradation and Fe^{3+} release, full degradation was reached within 7 days. This accelerated degradation and release can be directly attributed to the more porous polymer network resulting from reduced cross-linking, which facilitated water penetration and promoted chain scission. Such tunable degradation and release characteristics allow the material's lifespan to be aligned with the typical stages of tissue regeneration. By modulating the $R_{Fe/cat}$ ratio, the degradation and release kinetics can be precisely controlled, ensuring that the hydrogel provides sufficient mechanical support and therapeutic intervention throughout the critical healing period. Moreover, the tensile strengths of TCMBAs crosslinked by $FeCl_3$ in bicine solution at pH 5.0 were significantly lower than those of the corresponding formulations at pH 7.5 (Fig. S5). This is likely due to impaired formation of iron-catechol coordination bonds at lower pH, consistent with the pH-dependent crosslinking mechanism. Based on the results shown in Fig. 1B and S5, the gelation temperature of TCMBA in the tumor microenvironment (pH ~6.5) should be lower than that in normal tissue (pH ~7.4), and acidic pH also would also lead to a lower cross-linking density for TCMBA. Therefore, at the same body temperature (37 °C), the TCMBA pre-crosslinking solution can undergo

gelation more rapidly and at an earlier stage upon entering the acidic tumor region, thereby promoting localized deposition and retention of TCMBA in this area and enhancing the precision and photothermal conversion efficiency. Meanwhile, the lower cross-linking density of TCMBA hydrogel facilitates faster drug diffusion at the tumor site, thus improving the inhibitory effect against tumor cells. This pH-responsive differential gelation behavior constitutes an intrinsic passive targeting strategy, which not only enables superior drug enrichment at tumor sites but also reduces the diffusion of the material into normal tissues, thereby enhancing therapeutic specificity and reducing systemic toxicity. Furthermore, the swollen TCMBA hydrogels still maintained elasticity and certain mechanical strengths (Table S2), enabling the practical application of TCMBAs on flexible and dynamic soft tissues under physiological conditions. In addition, as shown in Fig. S6, the mechanical compression test results of TC-Fe1/9 over 7 days at 37 °C indicate that its compressive stress–strain behavior remains stable across different time points (0, 3, and 7 days). This demonstrates that the TCMBA material possesses favorable mechanical stability and structural durability under simulated physiological temperature conditions.

Benefiting from the reversible iron-catechol coordination and –COO^-—Ca^{2+}/Fe^{3+}–^-OOC– ionic bonds, TCMBAs exhibited a favorable self-healing evidenced by the successful fusion of cut film pieces and corresponding SEM observations (Fig. 2F). This capability was further supported by the rheological test results shown in Fig. 2G. After application of a large oscillatory strain (1000%) for 1 min, the storage modulus (G′) of TC-Fe1/9 recovered almost completely within approximately 1 min upon relaxation (1% strain), even after four successive cycles. Furthermore, the TCMBAs exhibit remarkable shape adaptability and high elasticity, enabling them to conform to and fill irregular wounds seamlessly (Fig. 2H), while maintaining strong adhesion to human skin under various mechanical challenges (Fig. 2I and Movie S3), including tensile, compressive, and torsional stresses. The strong adhesion to human skin is primarily attributed to the mussel-inspired catechol groups present in the iC-E-Ca^{2+} prepolymer. To systematically evaluate the adhesive properties, TCMBA was further applied to various substrates—including plastic, glass, metal, and biological tissues—and the results consistently demonstrated robust and versatile bonding capabilities (Fig. 2J). Lap-shear testing using porcine skin was further conducted to quantitatively evaluate the adhesive strength of TCMBA (Fig. 2K). The adhesion strengths of all tested TCMBAs to porcine skin were significantly higher than that of fibrin glue (<5 kPa), which is regarded as the gold-standard tissue adhesive (Fig. 2L). Moreover, lower $FeCl_3$ concentrations yielded higher adhesion strengths, with TC-Fe1/12 exhibiting a strength of approximately 27 kPa, compared to approximately 10 kPa for TC-Fe1/3. This inverse correlation occurs because a higher Fe^{3+} concentration, while increasing crosslinking density and cohesion strength, consumes catechol groups, thereby diminishing their availability for interfacial adhesion. The SEM micrographs display a highly cohesive and filamentous morphology, with the matrix forming an interconnected network of filaments (Fig. S7). This network structure, composed of polymer chains subjected to varying degrees of stretching and entanglement, directly visualizes the TCMBA's strong adhesion and cohesion.

3.1.4. Cytocompatibility of TCMBAs

The cytocompatibility of TCMBAs was evaluated using cytotoxicity assays of their soluble extracts and degradation products, along with a cell proliferation assay against mouse fibroblast (L929) cells. As shown in Fig. S8A, the soluble extracts from all tested TCMBAs exhibited mild cytotoxicity at 1 × concentration, resulting in cell viabilities between 60% and 80%; these values increased with dilution. Although treatment with 1 × degradation products resulted in cell viabilities below 40% for all TCMBAs (Fig. S8B), these values were comparable to those obtained with poly(lactic-co-glycolic acid) (PLGA) (~43.0 %), an FDA-approved biocompatible polymer widely used in clinical applications. With the exception of the 10 × degradation product of TC-Fe1/3 (<50% viability), all 10 × and 100 × degradation products from other groups supported cell viabilities above 85%, with some exceeding 100% (Fig. S8B). Live/Dead staining images of L929 cells (Fig. S8C) further confirmed that all TCMBAs except TC-Fe1/3 promoted cell densities and spreading morphologies comparable to those in the control and PLGA groups. Together, these findings indicate that the cytotoxicity of TCMBAs is concentration-dependent and appears to be influenced by Fe^{3+} content, with the formulation containing the highest Fe^{3+} level (TC-Fe1/3) showing the most pronounced effects. This underscores the need to optimize the Fe^{3+} concentration to achieve an optimal balance between material properties and biocompatibility.

3.2. Photothermal performance and photothermal antimicrobial & anticancer properties of TCMBAs

3.2.1. Intrinsic Photothermal Performance of TCMBAs

The presence of mussel-inspired catechol groups and their coordination with Fe^{3+} ions endow TCMBAs with a robust intrinsic photothermal effect. Upon 808 nm NIR irradiation at a power density of 0.50 W/cm^2, all the tested TCMBA dry films showed a fast temperature rise in the first 3 min, followed by stabilization at a platform stage (Fig. 3A and B). The photothermal heating was highly localized, with the temperature increase confined precisely to the laser-irradiated areas for all TCMBAs (Fig. 3A). TCMBAs exhibited significantly faster and higher temperature rise (ΔT) than those of iC-E-Ca^{2+} prepolymer and iC-8% PI (crosslinked with 8 wt% sodium periodate (PI) [34], indicating that the inclusion of Fe^{3+} greatly improved the photothermal conversion efficiency (Fig. 3B). The temperature-time curves of TC-Fe1/3, TC-Fe1/6, and TC-Fe1/9 were nearly superimposable, despite their differing Fe^{3+} contents (Fig. 3B). Therefore, considering potential long-term biocompatibility, TC-Fe1/9 (with the lowest Fe^{3+} content) was selected for subsequent experiments. The high photothermal conversion efficiency and tunability of TCMBAs were further demonstrated: increasing the NIR power density from 0.25 to 0.75 W/cm^2 raised the equilibrium temperature of TC-Fe1/9 from 36.0 to 82.0 °C (Fig. 3C). Moreover, TCMBAs exhibited a highly repeatable photothermal performance, as reflected by the fact that TC-Fe1/9 maintained the same temperature increase trend and retained most of its ΔT even after four consecutive cycles of 5-min NIR irradiation (0.5 W/cm^2) and free cooling cycles (Fig. 3D). Notably, upon NIR irradiation, wet TC-Fe1/9 exhibited a thermal-induced decolorization effect at ~45 °C (Fig. 3E and Movie S4). Although the temperature rise continued when the decolorized hydrogel turned black again followed by precipitation from the system, the temperature finally stabilized at ~52 °C. The thermally induced decolorization effect and the final precipitation of TCMBAs slowed down the temperature rise rate, conferring TCMBAs with mild PTT potential. In summary, TCMBAs combine rapid photothermal heating, excellent spatial localization (low thermal diffusion), and stable cyclability, making them promising candidates for photothermal applications where precise thermal delivery is crucial.

The photothermal performance of TCMBAs was further studied *in vivo* by subcutaneously injecting and thermal crosslinking TC-Fe1/9 in the back of Sprague-Dawley (SD) rats followed by 808 nm NIR irradiation for 10 min (0.5 W/cm^2). Fibrin glue injected and untreated SD rats were used as controls. Upon NIR irradiation, the temperature of the TC-Fe1/9+NIR group quickly rose to an equilibrium temperature of ~48 °C after 3 min and stabilized, while the control and Fibrin glue + NIR groups showed no change in temperature (Fig. 3F and G). Due to skin and tissue attenuation, the maximum photothermal temperature achieved *in vivo* (~48 °C) was ~5 °C lower than that of the *in vitro* result. It is reported that a temperature ~50 °C or higher is able to denature proteins and kill microbes, but high temperature might cause inflammation and thermal damage to nearby tissues [44,52]. However, cell damage, such as apoptosis, at a lower temperature can be repaired. The equilibrium temperature of ~48 °C is sufficient for PTT without causing excessive damage to surrounding tissues. Moreover, the photothermal

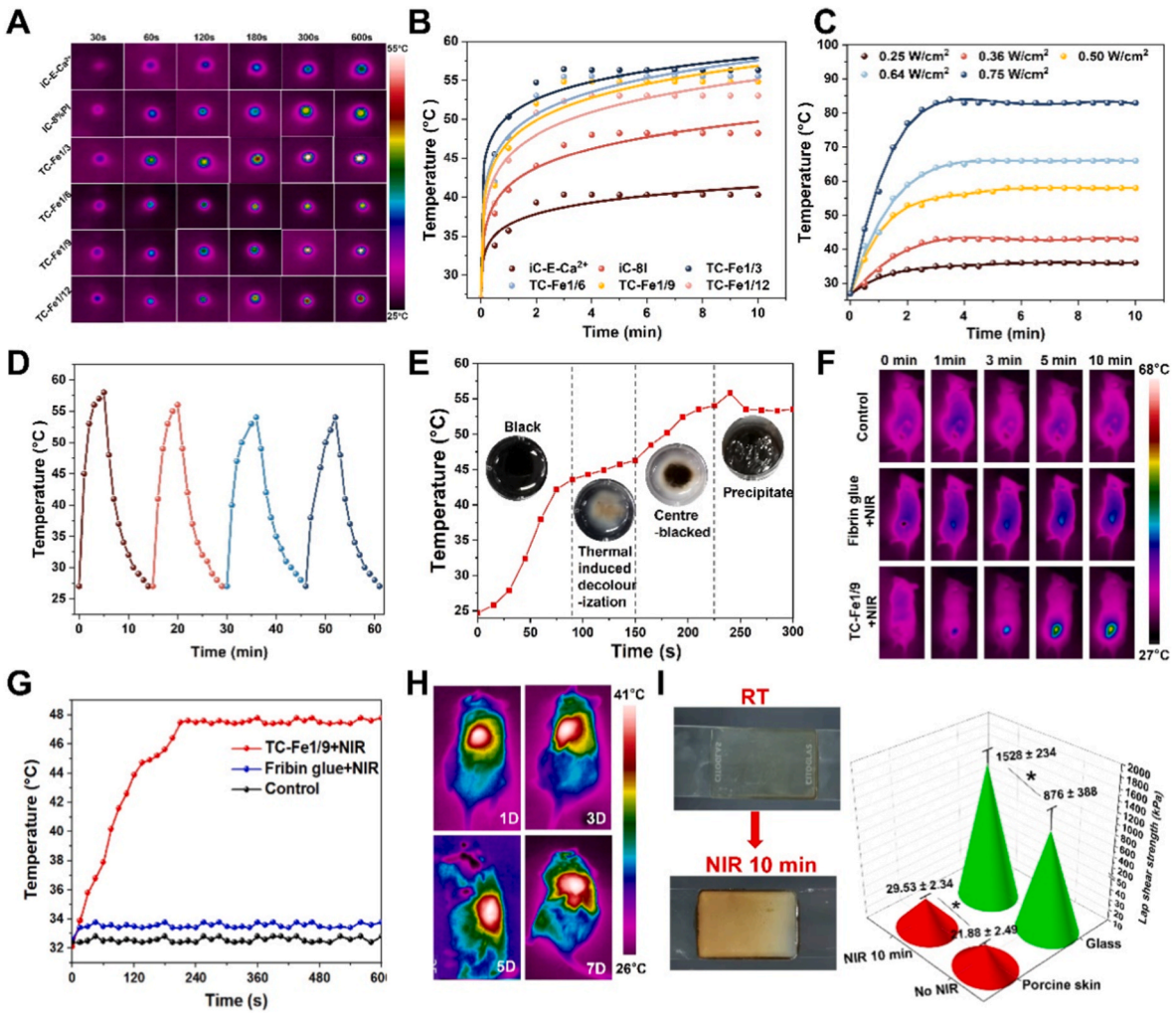

Fig. 3. Photothermal performance of TCMBAs. **A)** Infrared thermal images of TCMBAs after irradiation with an 808 nm NIR laser at 0.5 W/cm^2 for 10 min. **B)** Time-dependent temperature profiles of various TCMBAs under irradiation (808 nm, 0.5 W/cm^2). **C)** Temperature elevation curves of TC-Fe1/9 under irradiation at different power densities (808 nm). **D)** Photothermal stability of TC-Fe1/9 assessed over four cycles of NIR laser switching (808 nm, 0.5 W/cm^2). **E)** Temperature curve of a hydrated TC-Fe1/9 hydrogel under NIR irradiation (808 nm, 0.5 W/cm^2). Insets show photographs of the hydrogel at indicated temperatures. **F)** Infrared thermal images of nude mice from different groups after 10 min of irradiation (808 nm, 0.5 W/cm^2). **G)** Corresponding time-dependent temperature curves for the regions of interest. **H)** Thermal images of mice after 5 min of irradiation (808 nm, 0.5 W/cm^2) at 1, 3, 5, and 7 days post-subcutaneous injection of TC-Fe1/9. **I)** Lap-shear adhesion strength of TC-Fe1/9 on porcine skin and glass substrates with/without NIR irradiation (808 nm, 0.5 W/cm^2)(n = 5).

efficacy of TC-Fe1/9 was maintained *in vivo* even after 7 days (Fig. 3H), further confirming the stability and potential of TCMBAs for mild PTT applications.

3.2.2. *The effect of NIR irradiation on the adhesion properties of TCMBAs*

The combination of photo-induced temperature elevation and thermosensitive gelation confers TCMBAs with special photo-induced changes in polymer chain entanglement, which are deemed to affect their adhesion properties. As shown in Fig. 3I, NIR irradiation significantly enhanced the tissue adhesion strength of TC-Fe1/9 to porcine skin, increasing it from 21.88 ± 2.49 kPa to 29.53 ± 2.34 kPa ($p < 0.05$). More strikingly, a sample of TC-Fe1/9 sandwiched between two glass slides transitioned from transparent to opaque and white upon NIR irradiation (inset, Fig. 3I), consistent with the NIR-induced decolorization phenomenon observed in Fig. 3E. Furthermore, the adhesion strength of TC-Fe1/9 to glass also increased significantly, from 876 ± 388 kPa to 1528 ± 234 kPa after irradiation (Fig. 3I). Therefore, the observed enhancement, rather than deterioration, of adhesion strength on both biological (porcine skin) and model (glass) substrates during and after irradiation demonstrates that the photothermal effect does not compromise the TCMBA's adhesive integrity. The concurrent NIR-induced adhesion enhancement phenomenon suggests a microstructural reorganization within the irradiated TCMBA, involving improved polymer chain diffusion and mobility due to localized heating. This temperature increase also triggers a conformational transition within the EPE block copolymer [53,54]. This reorganization leads to increased polymer chain mobility and crosslinking density, resulting in a more cohesive and robust network that uniformly strengthens the adhesive interface. In conclusion, the photothermal process not only enables therapeutic functions but also actively improves the adhesive and sealing performance of TCMBAs, ensuring maintained adhesion and sealing integrity throughout the photothermal treatment. This NIR-induced enhancement of adhesion strength is particularly beneficial for the PTT application of TCMBAs in complex wounds, where robust and durable tissue adhesion is required.

3.2.3. *The in vitro Photothermal antimicrobial & anti-cancer Properties of TCMBAs*

The *in vitro* photothermal antimicrobial and anticancer activities of TCMBAs were assessed using a Transwell co-culture system (Fig. 4A). In-situ thermally crosslinked TCMBA (represented by TC-Fe1/9) was placed in the upper chamber, while bacteria (*Staphylococcus aureus*

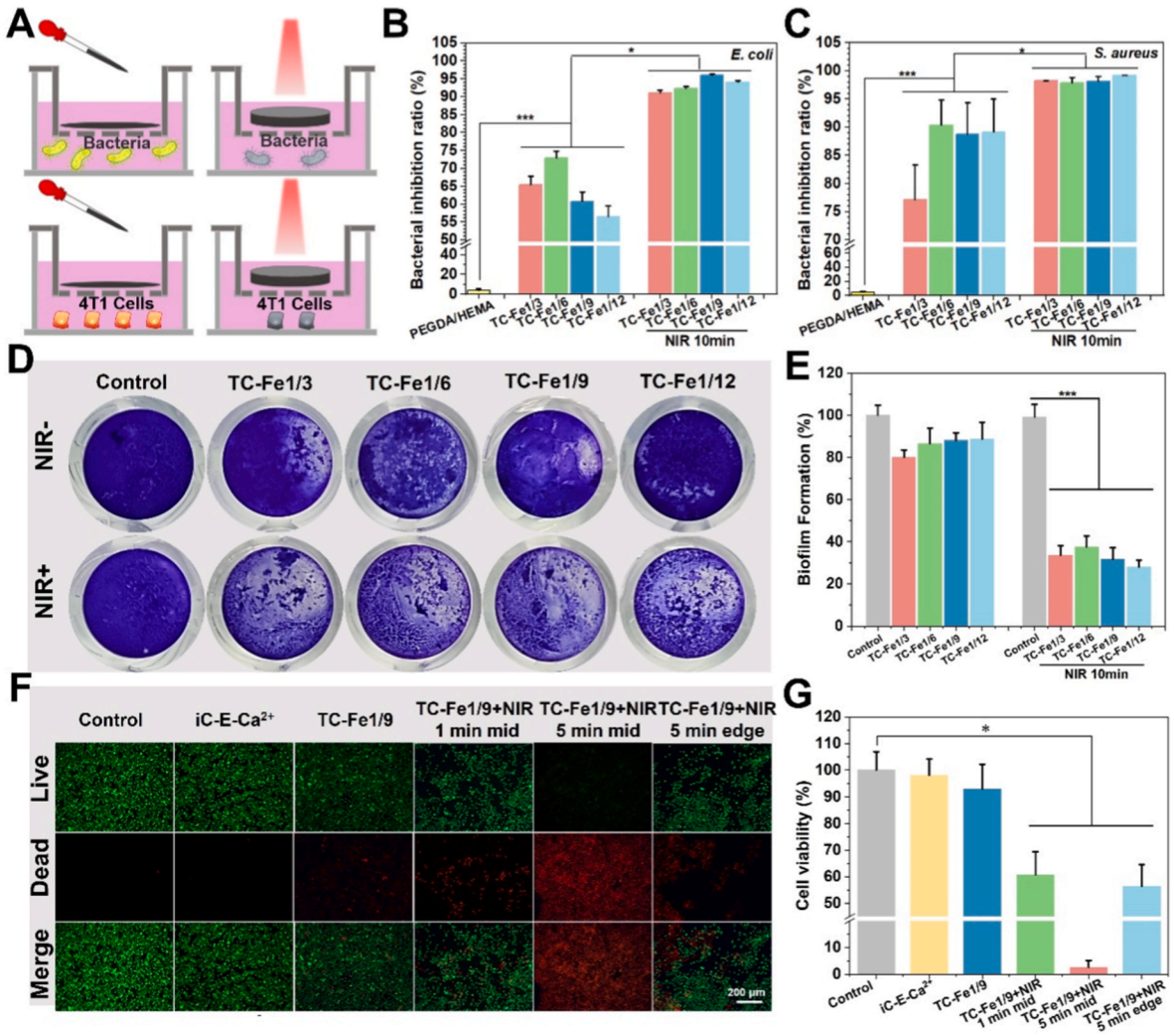

Fig. 4. Photothermal therapy (PTT) performance of TCMBAs. **A)** Schematic illustration of the experimental setup for evaluating the photothermal antibacterial and anticancer efficacy of TCMBAs. Bacterial inhibition ratios against **B)** *E. coli* and **C)** *S. aureus* for TCMBAs with/without NIR irradiation (0.5 W/cm^2, 10 min), using a non-antimicrobial PEGDA/HEMA hydrogel as a negative control (n = 3). **D)** Representative crystal violet-stained images and **E)** quantitative analysis of *S. aureus* biofilm formation after treatment with TCMBAs with/without NIR irradiation (n = 3). **F)** Live/Dead staining images and **G)** cell viability of 4T1 cells treated with TC-Fe1/9 with/without NIR irradiation (808 nm, 0.5 W/cm^2) (n = 5). $^*p < 0.05$, $^{**}p < 0.01$, $^{***}p < 0.001$.

(*S. aureus*) and *Escherichia coli* (*E. coli*)) or murine breast cancer 4T1 cells were cultured in the lower chamber. The hydrogel was then irradiated with an 808 nm NIR laser at 0.5 W/cm^2 for 10 min. Compared with PEGDA/HEMA (crosslinked hydrogel of poly(ethylene glycol) diacrylate (750 Da) and 2-hydroxyethyl methacrylate [30], used as a non-antibacterial control), TCMBAs showed considerable intrinsic antibacterial activity, especially against *S. aureus* (bacterial inhibition ratio = 77–90%, Fig. 4B and C). In contrast, the antibacterial activity of TCMBAs against *E. coli* was slightly weaker (56–73%). After NIR irradiation for 10 min, all TCMBAs exhibited nearly complete (>99%) antibacterial activity against both strains (Fig. 4B and C). This result is consistent with previous literature reports that temperatures at or above 50 °C are lethal to bacteria [55]. The perfect photothermal antibacterial activity of TCMBAs was further confirmed by the observation that the turbid bacterial suspensions became transparent after NIR irradiation (Fig. S9). Having established the efficacy against planktonic bacteria, we next evaluated the ability of TCMBAs to inhibit biofilm formation under NIR irradiation using a crystal violet staining assay. The crystal violet staining assay was employed to quantitatively evaluate the inhibitory effect of TCMBAs on bacterial biofilm formation under NIR laser irradiation. As shown in Fig. 4D and E, both control groups (NIR- and NIR+) exhibited intense purple staining, indicating robust biofilm formation. In contrast, the staining intensity decreased with increasing $R_{Fe/cat}$ in the groups treated with TCMBAs alone. Notably, the most pronounced biofilm eradication was observed in groups subjected to combined treatment with TCMBAs and NIR irradiation (NIR+). Under NIR laser exposure, TCMBAs generated substantial localized heat, leading to effective disruption of the biofilm matrix. The effect of individual components and treatment methods on bacteria was investigated (Fig. S10). It was found that single components (e.g., citric acid, ferric chloride) and the iC-E-Ca^{2+} solution exhibited certain inhibitory effects against both types of bacteria, though their efficacy was relatively limited. The TC-Fe1/9 hydrogel demonstrated strong antibacterial activity even in the absence of NIR irradiation. When combined with NIR irradiation (TC-Fe1/9+NIR), its antibacterial effect was further enhanced, indicating that the photothermal effect could synergistically improve the antimicrobial performance of the hydrogel. The control group treated at 48 °C for 10 min also showed significant antibacterial activity, although the effect was slightly lower than that of the TC-Fe1/9+NIR group, further confirming that thermal treatment inhibits bacterial growth and supporting the rationale for combining photothermal therapy. Therefore, the TC-Fe1/9 hydrogel demonstrated exceptional broad-spectrum antibacterial potential, which results in nearly complete bacterial inhibition, especially when combined with

NIR irradiation. Its mechanism of action is closely related to the inherent chemical antibacterial properties of TCMBAs and their photothermal conversion capability. These results confirm the role of TCMBAs as highly efficient photothermal agents and demonstrate that their combination with NIR irradiation offers an effective and non-invasive approach to combat bacteria.

The photothermal anti-cancer efficacy of TCMBAs was subsequently evaluated. As shown in Fig. 4F and G, without NIR irradiation, compared to the control and iC-E-Ca^{2+} groups, TC-Fe1/9 exhibited only a mild killing effect on 4T1 cells, which was deemed to be derived from Fe^{3+} and citrate as indicated in the cytotoxicity results (Fig. S8). Upon NIR irradiation (808 nm, 0.5 W/cm2), the 4T1 cells treated with TC-Fe1/9 began to die after 1 min, exhibiting a viability rate of 62.5%. A 5-min NIR irradiation was sufficient to kill all 4T1 cells directly underneath the irradiation spot (labeled as “mid” in Fig. 4F), resulting in a cell viability below 10%. In contrast, cells at the edge of the irradiation spot (labeled as “edg” in Fig. 4F) remained partially viable, with a survival rate of 58.4%. These *in vitro* findings substantiate the dual photothermal antimicrobial and anticancer efficacy. The observed activity appears to involve a combination of thermally mediated mechanisms initiated by local hyperthermia (>50 °C), including direct damage to tumor/microbial membranes and heat-induced mitochondrial dysfunction [56]. Concurrently, hyperthermic conditions likely disrupt critical cellular processes such as DNA replication and RNA synthesis. Additionally, the inherent biological activities of Fe^{3+} and citrate synergistically contribute to the overall therapeutic outcome [57,58].

3.3. In Vivo therapeutic performance of TCMBAs in complex wounds

To achieve a comprehensive optimization of the TCMBA's therapeutic efficacy, application performance, and biosafety, TC-Fe1/9 was ultimately selected as the representative system for further investigation. Although the tensile strengths of TC-Fe1/9 and TC-Fe1/12 were slightly lower than that of TC-Fe1/3 and TC-Fe1/6, the higher elongations at break of TC-Fe1/9 and TC-Fe1/12 indicate superior elasticity. Moreover, possessing more free catechol groups, the tissue adhesion strengths of TC-Fe1/9 and TC-Fe1/12 were higher than those of TC-Fe1/3 and TC-Fe1/6. On the other hand, benefiting from their lower Fe^{3+} concentrations, TC-Fe1/9 and TC-Fe1/12 demonstrated superior cytocompatibility compared to TC-Fe1/3 and TC-Fe1/6. Finally, TC-Fe1/9 possesses lower sol content and swelling ratio than that of TC-Fe1/12, which is beneficial to maintain the structural stability and mechanical properties of the hydrogel, thereby avoiding potential tissue damage or uncontrolled release caused by excessive swelling. Overall, TC-Fe1/9 achieved an optimal balance in biocompatibility, structural stability, and key application properties while maintaining satisfactory photothermal therapeutic performance, thus it was chosen as the representative TCMBA for the subsequent *in vivo* experiments.

3.3.1. In vivo hemostatic capability and hemocompatibility of TCMBAs

Adhesive hydrogels can be employed for wound closure, where they act as a physical barrier to achieve hemostasis [8–11]. Furthermore, the calcium ions (Ca^{2+}) conjugated to the side chains of the iC-E-Ca^{2+} prepolymer are anticipated to enhance the hemostatic efficacy of TCMBAs, given the well-established role of Ca^{2+} as an essential cofactor in the coagulation cascade [59]. The hemostatic performance of TCMBAs (using TC-Fe1/9) was assessed by a Sprague-Dawley (SD) rat tail amputation model. The effective hemostatic capability is demonstrated in Fig. S11. Compared to the control group (hemostatic time: 488 ± 55 s; blood loss: 0.799 ± 0.11g), the Fibrin glue group showed a significantly shorter hemostatic time (217 ± 36s, $p < 0.001$) and reduced blood loss (0.19 ± 0.08g, $p < 0.001$). In contrast, the TC-Fe1/9 group demonstrated even more pronounced hemostatic effects, with the hemostatic time further shortened to 183 ± 29 s ($p < 0.001$) and blood loss reduced to 0.18 ± 0.03g ($p < 0.001$) (Fig. S11). These results may be attributed to the adhesive sealing effect of TC-Fe1/9 and the promotion of the coagulation process by the released calcium ions, which together contribute to its superior overall hemostatic performance. In summary, TC-Fe1/9 exhibits favorable effects in both reducing blood loss and shortening hemostatic time, suggesting its potential as a novel adhesive hemostatic material for acute hemorrhage control [10].

Additionally, the hemocompatibility of TCMBA has been tested. As shown in Fig. S12, the positive control group (0.1% Triton X-100) exhibited a marked hemolytic effect, with a hemolysis rate of 100%. In contrast, the hemolysis rate in the negative control group (PBS) was only 1.47%, confirming the reliability of the experimental system. Compared to the PBS group, the hemolysis rates in the fibrin glue group and the TC-Fe1/9 group were 1.71% and 2.39%, respectively, indicating no significant hemolysis. These values are well below the internationally recognized safety threshold of 5%. Therefore, these results demonstrate that TCMBAs possess favorable hemocompatibility and meet the safety requirements for biomaterials.

3.3.2. In vivo infection wound healing Performance of TCMBAs

The *in vivo* wound healing performance of TCMBAs was assessed using an infected full-thickness skin arc-incision model in mice, which was created by injection with *S. aureus* (Fig. 5A). After three days of treatment, the residual bacteria on the infected skin wounds were collected and plated on agar plates for colony counting (Fig. 5B and C). Compared with the Suture and Fibrin glue groups, the TC-Fe1/9 group showed certain antibacterial activity, which was further enhanced with the assistance of NIR irradiation. The number of residual *S. aureus* colonies in the TC-Fe1/9+NIR group was significantly lower than that in the suture and fibrin glue groups ($p < 0.001$) and was comparable to that in the uninfected group (Fig. 5C). This result demonstrates the potent *in vivo* antimicrobial efficacy of the TCMBA-based photothermal therapy. As shown in Fig. 5D, the overall healing rates of infected wounds were slower than those of uninfected wounds. Furthermore, the skin surrounding the wounds in the suture and fibrin glue groups exhibited erythema (redness) and tissue damage, particularly during the first week, which is attributable to the lack of effective antibacterial activity. The robust tissue adhesiveness of TCMBAs ensured effective wound sealing in both the TC-Fe1/9 and TC-Fe1/9+NIR groups. In contrast, gaps at the wound site were evident in the suture and fibrin glue groups at days 3 and 7 post-operation (Fig. 5D). On day 14, although the TC-Fe1/9 and TC-Fe1/9+NIR groups exhibited lower wound healing rates than the uninfected group, their residual incision lengths were significantly shorter than those in the suture and fibrin glue groups (Fig. 5E). This indicates that incorporating antimicrobial capability into tissue adhesives promotes the healing of infected wounds. Taken together, these results further confirmed the intrinsic (derived from citrate and Fe^{3+}) and photothermal antimicrobial activity of TCMBAs *in vivo* and preliminarily demonstrated the wound healing accelerating efficacy of TCMBA and TCMBA + NIR on infected wounds.

The effect of TCMBAs treatment (±NIR) on infected wound healing was further investigated by performing histological staining, including hematoxylin and eosin (H&E) and Masson's trichrome, and immunofluorescence staining for collagen type I alpha 1 (COL1A1) and platelet endothelial cell adhesion molecule-1 (CD31). These analyses assessed key processes including re-epithelialization, connective tissue formation, collagen deposition, and neovascularization. As shown in Fig. 5F, on day 7, the wounds in all infected groups remained in an early inflammatory phase, characterized by acute inflammatory infiltration and granulation tissue formation. At this time point, re-epithelialization was minimal and collagen deposition sparse. However, the TC-Fe1/9 and TC-Fe1/9+NIR groups demonstrated greater fibroblast recruitment and significantly enhanced collagen deposition compared to the suture and fibrin glue groups. These differences are evident in the larger blue-stained areas (Masson's trichrome) and more intense green fluorescence (COL1A1) observed in these groups (Fig. 5F–S13, and S14). Although all infected groups exhibited less neovascularization than the uninfected group on day 7, the TC-Fe1/9 (±NIR) treatment resulted in

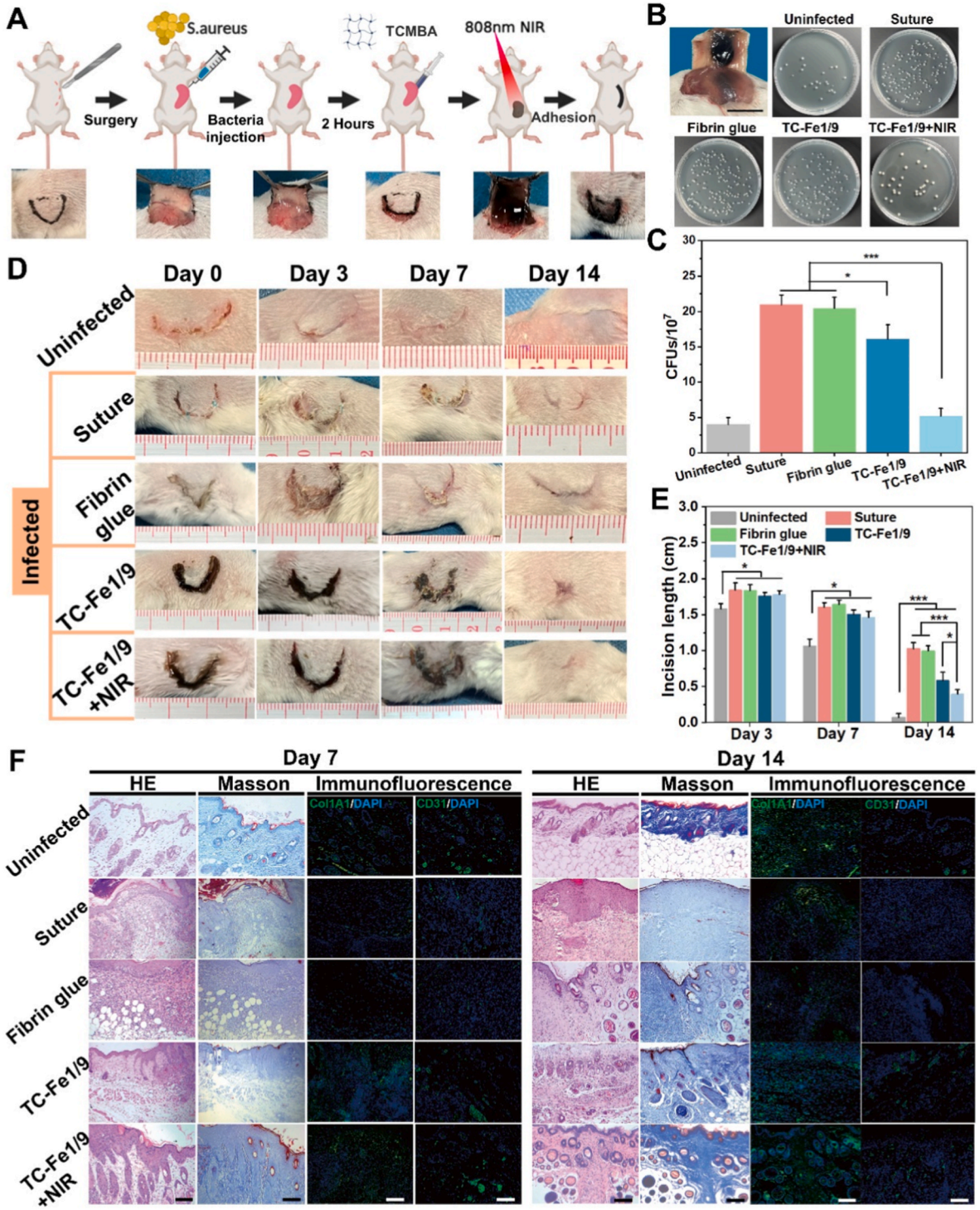

Fig. 5. Evaluation of TCMBA-mediated wound healing in an infected full-thickness skin incision model. A) Schematic illustrating the establishment of the infected animal model and the subsequent administration of TCMBA (TC-Fe1/9) with NIR photothermal therapy. **B)** Representative photographs and **(C)** quantitative analysis of colony-forming units (CFUs) of viable *S. aureus* collected from the infected incision sites 3 days post-operation (n = 5). **D)** Representative wound healing photographs of the treated incisions on days 0, 3, 7, and 14 and **E)** the corresponding incision lengths (n = 5). **F)** H&E, Masson's trichrome, and immunofluorescent (Col1A1 and CD31) staining images, scale bar = 100 μm $*p < 0.05$, $**p < 0.01$, $***p < 0.001$.

significantly greater angiogenesis compared to the suture and fibrin glue groups (Fig. 5F and S15). On day 14, the wounds in all five groups had closed completely. However, the suture and fibrin glue groups exhibited disorganized fibrous tissue and fewer skin appendages. In contrast, the uninfected, TC-Fe1/9, and TC-Fe1/9+NIR groups exhibited complete re-epithelialization and the formation of numerous new hair follicles. This was particularly evident in the uninfected and TC-Fe1/9+NIR groups, which also displayed restored skin architecture and nearly scarless tissue. On day 14, the wounds were substantially healed and exhibited a structure similar to normal skin, with further increased collagen deposition. Quantitatively, the collagen densities and COL1A1-positive staining percentages in the TC-Fe1/9 and TC-Fe1/9+NIR groups were significantly higher ($p < 0.05$) than those in the suture and fibrin glue groups (Fig. 5F–S13, and S14). However, in the uninfected group, a

subcutaneous fat layer was observed and the epithelium was thinner than that in the infected groups, resulting in a lower overall collagen density throughout the Masson's trichrome-stained sections. Although CD31 expression decreased on day 14 compared to day 7, a trend consistent with normal skin remodeling, the two TC-Fe1/9 groups still exhibited significantly more extensive neovascularization than the suture and fibrin glue groups (Fig. 5F and S15). Moreover, a biomechanical study of the healed skin tissues was conducted and compared with normal skin tissues 14 days after the operation. Although the tensile strengths of the TC-Fe1/9 and TC-Fe1/9+NIR groups were lower than

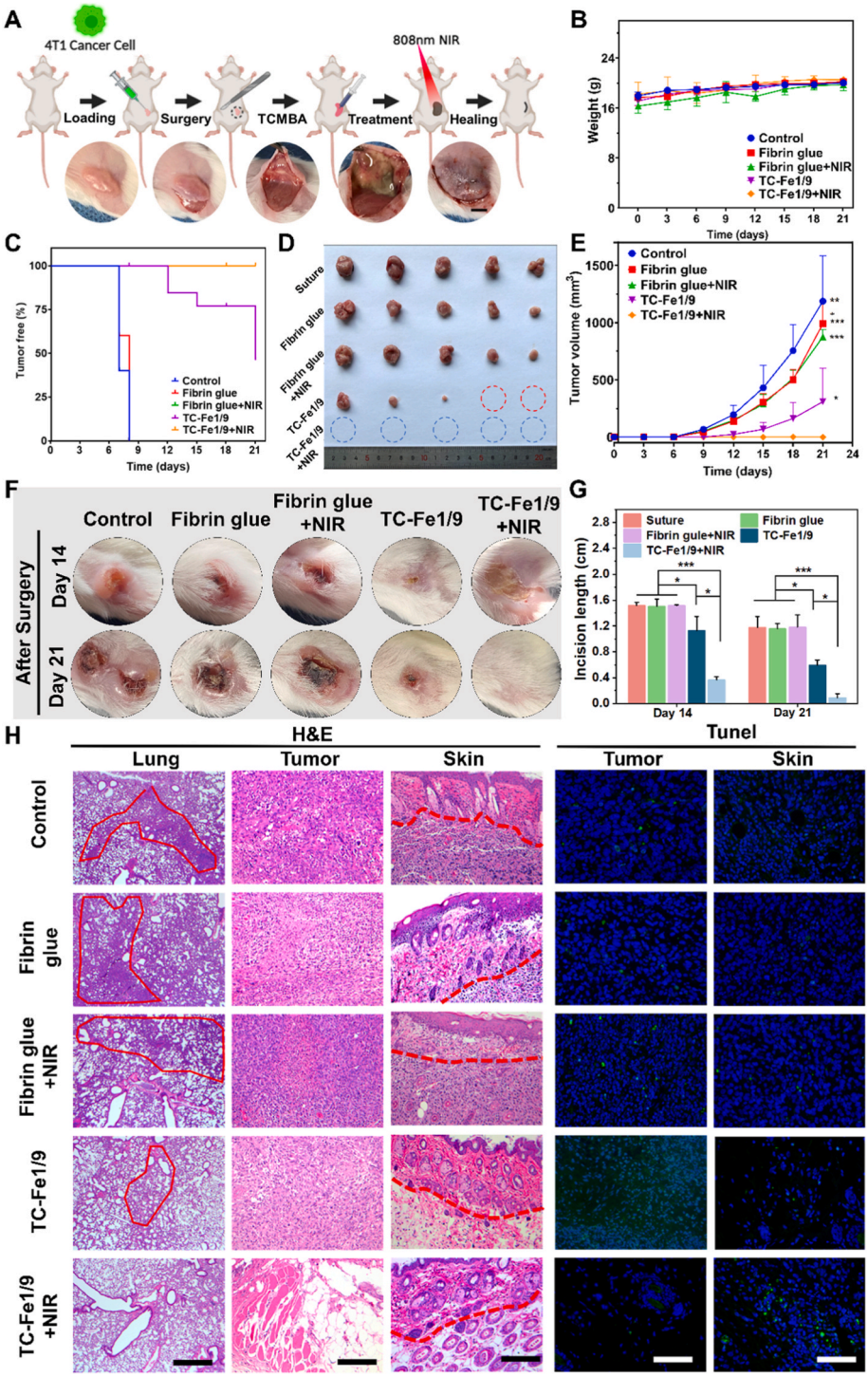

Fig. 6. Evaluation of TCMBA-mediated prevention of tumor recurrence and promotion of wound healing in a post-surgical cancerous wound model. A) Schematic illustrating the establishment of the post-surgical recurrence model and the subsequent treatment protocol with TCMBA (TC-Fe1/9) with or without PTT. **B)** Body weights of mice measured throughout the study period to assess systemic toxicity (n = 5). **C)** Tumor-free rates (n = 5). **D)** Representative photographs of excised recurrent tumors and **(E)** quantitative analysis of recurrent tumor volumes on day 21 (n = 5). **F)** Representative photographic documentation of wound appearance on days 14 and 21 post-surgery. **G)** Quantitative measurement of wound closure, presented as incision length on days 14 and 21 (n = 5). **H)** H&E staining images of lung, tumor, and skin tissues, and TUNEL staining images of the excised recurrent tumors and surrounding skin tissues on day 21, scale bar = 100 μm $^{*}p < 0.05$, $^{**}p < 0.01$, $^{***}p < 0.001$.

those of the uninfected group and normal skin, they were significantly higher than those of the suture and fibrin glue groups ($p < 0.05$, Fig. S16).

Collectively, the above results indicate that compared with surgical sutures and fibrin glue, TCMBAs demonstrate superior wound healing effects in the infected full-thickness skin arc-incision model. This advantage may primarily stem from the synergistic mechanisms of the following aspects: Firstly, TCMBAs possess suitable tissue adhesion, enabling tight and durable wound closure, thereby maintaining structural stability in the dynamic wound environment [60]. The strong wound adhesion not only reduces tension resistance during healing but also blocks microbial invasion and provides a scaffold for cell migration, thereby significantly promoting granulation tissue formation [61]. Furthermore, the high water content of TCMBAs hydrogel helps maintain a moist wound environment, reducing the risks of tissue dehydration and contraction, which accelerates epithelial regeneration [62,63]. For the intrinsic healing-promoting effects of the material, the active components in TCMBAs, such as dopamine and citrate, can be continuously released locally and directly drive the tissue repair process by modulating inflammatory responses, promoting angiogenesis, improving cellular metabolism, and enhancing collagen deposition [64–66]. Particularly important is the photothermal antibacterial capability of TCMBAs, which effectively controls wound infection, inhibits biofilm formation, and alleviates the inflammatory microenvironment, thereby creating a favorable condition for wound healing [37,67,68]. In summary, through an integrated "attack–defense–treatment" synergistic mechanism, TCMBAs significantly accelerate the healing of infected wounds and exhibit promising potential for clinical translation.

3.3.3. *In vivo PTT efficacy to Prevent tumor recurrence and metastasis and Promote wound healing*

To evaluate the efficacy of TCMBAs in preventing tumor recurrence and metastasis and in promoting wound healing, a mouse model was established. Briefly, 4T1 cells were subcutaneously injected into the right flank of BALB/c nude mice. Once the tumor volume reached approximately 100 mm^3, the tumors were surgically excised to create full-thickness wounds (Fig. 6A). These wounds were then treated with one of five methods: surgical suture, fibrin glue, fibrin glue with NIR irradiation, TCMBA (TC-Fe1/9), or TCMBA (TC-Fe1/9) with NIR irradiation ($n = 5$). For the groups receiving NIR irradiation (Fibrin glue + NIR and TC-Fe1/9+NIR), wounds were closed with the respective material and then immediately irradiated with an NIR laser (808 nm, 0.5 W/cm^2) for 10 min. As shown in Fig. 6B, the body weights of all mice remained within a normal range (16–20 g) throughout the experimental period and no significant differences in weight change trends were observed among the groups, indicating the absence of overt systemic toxicity from the treatments [69]. However, by day 21, tumor recurrence was observed to varying degrees in all groups except the TC-Fe1/9+NIR group (Fig. 6C and D). The considerable efficacy of TC-Fe1/9 in preventing tumor recurrence may be attributed to the combined action of Fe^{3+}, which is a widely recognized inducer of ferroptosis in cancer cells, and citrate, which may promote apoptosis [10,39,70]. While only 40% of the mice in the TC-Fe1/9 group remained tumor-free by day 21, all mice in the TC-Fe1/9+NIR group maintained complete tumor-free survival (Fig. 6C–E). This result highlights the markedly enhanced therapeutic efficacy conferred by NIR-triggered photothermal therapy. Moreover, the incision lengths in both the TC-Fe1/9 group ($p < 0.05$) and the TC-Fe1/9+NIR group ($p < 0.001$) were significantly shorter than those in the suture, Fibrin glue, and Fibrin glue + NIR groups (Fig. 6F and G). This demonstrates the superior wound healing efficacy of TCMBAs, which was further enhanced by NIR irradiation. In summary, the combination of TCMBA and photothermal therapy (PTT) not only effectively promotes wound closure and healing but also prevents post-resection tumor recurrence.

To further investigate the therapeutic efficacy of TCMBAs in post-surgical cancerous wounds and to elucidate the relationship between wound inflammation and tumor recurrence/metastasis, we performed histological (H&E), Tunel (terminal deoxynucleotidyl transferase-mediated dUTP-digoxigenin nick-end labeling), immunofluorescence (for tumor necrosis factor-α (TNF-α), CD31, CD86, and CD206), and immunohistochemical (for IL-1β and IL-10) staining on harvested wound tissues, tumor tissues, and major organs, followed by comprehensive analysis. Analysis of H&E and Tunel staining revealed that TC-Fe1/9 treatment significantly decreased the number of residual cancer cells and enhanced tumor cell apoptosis (Fig. 6H). Additionally, in sharp contrast to the control, Fibrin glue, and Fibrin glue + NIR groups, which showed comparable numbers of larger lung metastatic nodules, the TC-Fe1/9 group demonstrated a marked decrease in both nodule number and sizes (Fig. S17). These observations suggest that TCMBAs may function as an adhesive barrier, contributing to hemostasis and immobilization of circulating tumor cells (CTCs). Additionally, the Fe^{3+} and citrate components released from TCMBAs are likely to play critical roles in inducing tumor cell death and suppressing invasion into epidermal layers as well as distant metastasis. In the TC-Fe1/9+NIR group, histological examination revealed no residual tumor tissue and only normal tissue architecture in the surgical area. The absence of metastatic lesions in H&E-stained lung tissues (Fig. 6H and S17) confirms the efficacy of TC-Fe1/9+NIR in eliminating residual tumor cells after resection. This complete local clearance translates to the effective prevention of both local tumor recurrence and distant metastasis by the combined TCMBA-PTT strategy. Furthermore, distinct wound healing outcomes were observed between treatment groups. Compared to the TC-Fe1/9+NIR group, which achieved complete tumor eradication and resulted in normal wound bed formation, all other groups exhibited tumor recurrence, leading to tumor-bearing wound sites. Within these tumor-bearing sites, insufficient inherent antitumor activity of the material permits uninhibited tumor cell proliferation, consequently yielding minimal necrotic/apoptotic cell expression. In contrast, the TC-Fe1/9 group demonstrated significantly delayed recurrence and sustained apoptotic activity within the residual tumor tissue. This phenomenon is attributed to a continuous antagonistic interaction between the recurrent tumor mass and the material's antitumor constituents (Fe^{3+}, citrate). Specifically, Fe^{3+} in the system can catalyze the generation of highly reactive hydroxyl radicals from hydrogen peroxide via a Fenton reaction, thereby triggering lipid peroxidation and ultimately inducing ferroptosis of tumor cells [71–73]. Meanwhile, citric acid serves as a key metabolic intermediate in the tricarboxylic acid cycle and exhibits a dual regulatory role in cellular metabolism [64,74]. On the one hand, by participating in the tricarboxylic acid cycle, it can enhance energy metabolism, regulate intracellular pH and ion homeostasis, thereby promoting the proliferation of normal cells [64]. On the other hand, it can also exert selective anti-tumor effects through multiple pathways. These include disrupting tumor cell energy metabolism homeostasis, inhibiting glycolysis, enhancing sensitivity to cytotoxic drugs, suppressing critical signaling pathways (such as the IGF-1R/AKT pathway), and competitively chelating essential intracellular metal ions [75–77]. These two mechanisms are not independent but may synergistically reinforce each other. The chelation of iron ions by citrate is expected to enhance their stability and catalytic efficiency within the tumor microenvironment, while the metabolic disturbances triggered by ferroptosis may further amplify the metabolic interference effects of citrate, thereby forming a synergistic antitumor cycle. In short, these findings collectively underscore the paramount importance of achieving near-total tumor cell clearance in the initial treatment phase. Sustained antitumor effects within an established tumor bed represent a therapeutically inefficient approach. Therefore, the optimal strategy to overcome the inherent difficulty in healing tumor-associated wounds is the aggressive conversion of the tumor bed into a normal tissue bed at the earliest opportunity.

Given the critical interplay between tumor and skin tissue during wound healing, our histological analysis encompassed not only the distinct tumor and dermal regions but was specifically complemented by

a comprehensive characterization of the transitional interface zone. Consistent with the tissue apoptosis (TUNEL) staining results (Fig. 6H), the TC-Fe1/9 group exhibited the highest TNF-α expression level (276.2 ± 20.72% of the suture group level), which was significantly higher than that in the suture (100.0 ± 43.10%), fibrin glue (90.3 ± 53.60%), and fibrin glue + NIR (106.1 ± 45.58%) groups (Fig. 7A and B), providing further evidence of the apoptosis-inducing effect of TC-Fe1/9 on tumor cells. In contrast, in the TC-Fe1/9+NIR group, where tumor recurrence was completely prevented, TNF-α expression was significantly lower than that in both the TC-Fe1/9 group ($p < 0.001$) and all other control groups ($p < 0.05$) (Fig. 7A and B). In contrast to the other groups, the TC-Fe1/9+NIR group showed a high density of hair follicles, indicative of normal skin regeneration. Consistent with the high tumor recurrence and metastasis rates observed in the suture, Fibrin glue, and Fibrin glue + NIR groups, the CD31 expression levels in these three groups were also significantly higher than those in the TC-Fe1/9 and TC-Fe1/9+NIR groups ($p < 0.001$ for all comparisons, Fig. 7C and D). The CD31 expression level in the TC-Fe1/9+NIR group was the lowest among all groups, suggesting that tumor angiogenesis was substantially inhibited, thereby potentially reducing the risk of distant metastasis. These results

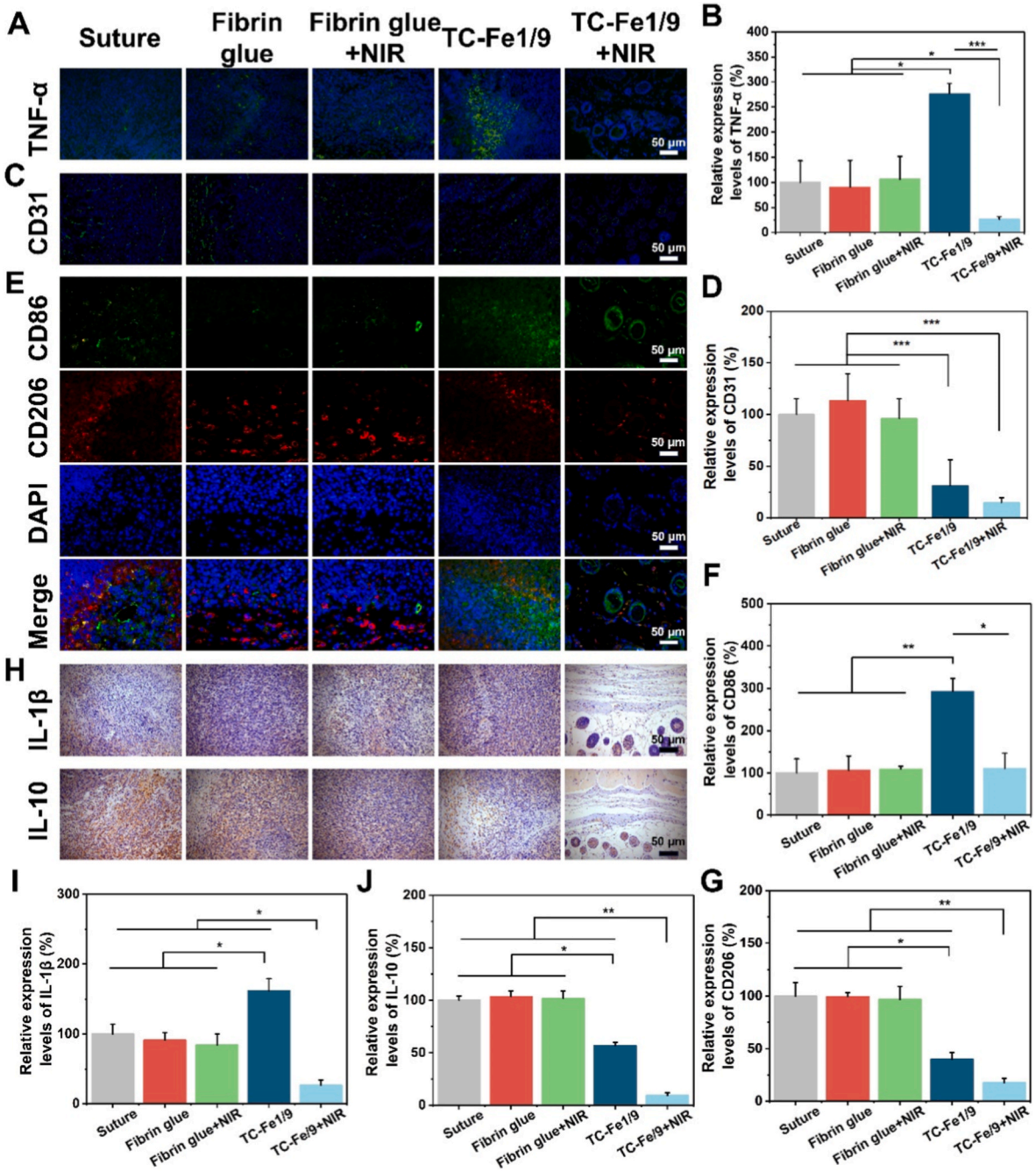

Fig. 7. Immune microenvironment analysis of the post-surgical tumor bed after treatment with TCMBA (TC-Fe1/9) with or without NIR. A) Representative immunofluorescence staining images of the tumor-skin junction on day 21 for TNF-α. **B)** The relative expression levels of TNF-α (n = 5). **C)** Representative immunofluorescence staining of CD31. **D)** The relative expression levels of CD31 (n = 5). **E)** Representative immunofluorescence staining images of CD86 (M1 macrophage marker) and CD206 (M2 macrophage marker). **F)** The relative expression levels of CD86 (n = 5). **G)** The relative expression levels of CD206 (n = 5). **H)** Representative immunohistochemical staining images of IL-1β and IL-10. The relative expression levels of **I)** IL-1β and **J)** IL-10 (n = 5). *$p < 0.05$, **$p < 0.01$, ***$p < 0.001$.

demonstrate that TCMBA, especially when combined with PTT, can effectively eliminate tumor recurrence and distant metastasis from post-surgical wounds while also promoting complete wound healing.

The opposite response of tumor and normal skin tissues to inflammation makes it difficult to synchronously kill tumor cells and promote wound healing. M2-type (anti-inflammatory) macrophages, which are highly expressed in tumor tissues, promote the growth and metastasis of tumor cells, while M1-type (pro-inflammatory) macrophages inhibit and kill tumor cells. However, for normal skin tissue, M2-type macrophages are favorable at the proliferation phase due to their wound healing promoting ability [37,78–80]. As shown in Fig. 7E and F, the CD86 (a marker for M1-type macrophages) expression level in the TC-Fe1/9 group was the highest among all groups (292.3 ± 30.80% of the suture control), which was significantly higher than that in the suture (100%), Fibrin glue, and Fibrin glue + NIR groups (100–111 %) ($p < 0.05$). This finding is consistent with the TUNEL (reflecting apoptosis) and TNF-α immunofluorescent staining data (Fig. 7A and B) and is further supported by the partial suppression of tumor recurrence in the TC-Fe1/9 group, in contrast to the suture, Fibrin glue, and Fibrin glue + NIR groups. Conversely, the suture, Fibrin glue, and Fibrin glue + NIR groups exhibited significantly higher expression levels of CD206 (a marker for M2-type macrophages) compared to the TC-Fe1/9 group ($p < 0.05$, Fig. 7E and G). When assisted by synergistic PTT, however, the TC-Fe1/9+NIR group achieved complete tumor cell eradication. This resulted in a macrophage distribution and histological morphology resembling normal skin tissue, characterized by moderate CD86 and relatively low CD206 expression. Moreover, as shown in Fig. S18, flow cytometry analysis of macrophages at tumor resection sites from each group showed results consistent with those obtained from immunofluorescence staining of CD86 and CD206 (Fig. 7E–G). In the control, Fibrin glue, and Fibrin glue + NIR groups, a higher proportion of M2 macrophages was observed, which may be associated with the maintenance of the tumor immune microenvironment (Fig. S18). In contrast, the TC-Fe1/9 group exhibited a predominance of M1 macrophages, suggesting disruption of the tumor microenvironment accompanied by tumor cell death. In the TC-Fe1/9+NIR group, due to the clearance of early-stage tumor tissue and the completion of tissue repair, levels of both M1 and M2 macrophages in the skin were notably lower. Moreover, the expression levels of inflammatory cytokines, including IL-1β (pro-inflammatory) and IL-10 (anti-inflammatory), in different groups also exhibited similar trends (Fig. 7H-J), further confirming TC-Fe1/9's ability to induce M1 polarization of macrophages in tumor tissues. Consequently, a comprehensive analysis of macrophage polarization (via CD86/CD206 immunofluorescence) and inflammatory cytokine expression (via IL-1β/IL-10 immunohistochemistry) reveals that TCMBA ± NIR treatment orchestrates a spatially-defined immunomodulatory strategy. It effectively reprograms the post-surgical immune microenvironment, fostering an anti-tumor response at the tumor site while establishing a pro-regenerative environment in the adjacent normal tissue. It thereby addresses the critical challenge of eliminating residual cancer while supporting wound healing.

The biocompatibility of the different treatments was assessed by evaluating the major organs (liver, spleen, kidney, and heart) using H&E staining. Examination of the H&E staining images revealed no significant pathological changes in any of the examined organs (Fig. S19), indicating the good biosafety profile of TCMBAs both with and without NIR irradiation.

The TCMBA platform represents a significant advance in both functional integration and therapeutic concept compared to current strategies for managing complex wounds. Whereas traditional dressings are mostly limited to providing either passive barrier protection or a single therapeutic function (e.g., hemostasis or antibacterial action alone), recently developed multifunctional material systems often exhibit insufficient integration of properties [81]. Common shortcomings include the frequent lack of robust tissue adhesion in thermosensitive hydrogels, the general absence of intelligently responsive therapeutic capabilities in mussel-inspired bioadhesives, and the particular difficulty of single-approach antibacterial or antitumor materials to address the complex clinical reality of co-existing infection and tumors [82,83]. Taking the extensively studied quaternary ammonium salt-based materials as an example, while they can disrupt microbial membrane structures via electrostatic interactions or induce cancer cell apoptosis, thereby exhibiting certain antibacterial and antitumor effects, their clinical translation potential is severely limited by several drawbacks [84]. These include inherent toxicity to normal cells, a single mechanism of action prone to inducing resistance, and poor biodegradability leading to persistent retention *in vivo* [85]. In contrast, the attack–defense system of TCMBA follows an intelligent, spatiotemporally coordinated process. Temporally, it first employs synergistic photothermal and chemodynamic therapies to precisely eliminate bacteria and tumor cells. Subsequently, as the photothermal effect ceases and the material undergoes metabolism, the therapeutic strategy dynamically shifts to a bioactive scaffold-driven repair phase. Spatially, the photothermal effect is confined to the material and its immediate surroundings, while its three-dimensional scaffold structure provides physical protection for subsequent normal tissue ingrowth and establishes a favorable regenerative microenvironment. This synergistic mechanism ensures high efficacy in sterilization and antitumor activity. By virtue of its localized action and non-reliance on the sustained release of toxic agents, it also effectively circumvents the biosafety risks and drug resistance issues common to conventional therapies. Although TCMBA elevates local temperature to 48 °C during treatment, the controllable duration and gradient-based thermal diffusion characteristics enable this photothermal therapy to effectively achieve antibacterial/antitumor outcomes while successfully avoiding significant thermal damage to surrounding healthy tissues.

Furthermore, compared to biologics such as antimicrobial peptides or anticancer agents (e.g., Keytruda, sparfloxacin), TCMBA's core components (citric acid, dopamine, and an iron source) are inexpensive and widely available [86,87]. Moreover, TCMBA can maintain its structural integrity in PBS at 37 °C for periods ranging from several days to weeks, with a degradation profile that can be tuned via its crosslinking density. Critically, *in vivo* experiments confirm that TCMBA effectively adheres to wounds and undergoes in-situ molding at body temperature, where it continues to function as a protective barrier for 7 days or longer. These attributes, which stem from its stable chemical structure, impart an extended shelf life and superior *in vivo* stability, affording TCMBA distinct advantages for clinical translation and large-scale production. In summary, TCMBA innovatively establishes an integrated attack–defense therapeutic paradigm. This system dynamically merges on-demand synergistic treatment (photothermal therapy) with active tissue repair functions (leveraging a citrate-based bioactive scaffold) within a single system. Consequently, it achieves coordinated management of infection control, tumor recurrence prevention, and wound healing promotion.

4. Conclusion

In summary, a family of thermosensitive citrate-based mussel-inspired bioadhesives (TCMBAs) was developed for the first time by simply mixing poly(ethylene glycol)-block-poly(propylene glycol)-block-poly(ethylene glycol)-incorporated and calcium-containing water-soluble injectable citrate-based mussel-inspired bioadhesive prepolymer (iC-E-Ca^{2+}) with $FeCl_3$ in bicine solution. The presence of the zwitterionic compound, bicine, is considered crucial for imparting thermosensitive gelation property to TCMBAs, and the difference in chelation manners between bicine and Fe^{3+} at acidic and basic pH is closely related to the pH sensitivity of the thermosensitive gelation property of TCMBAs. The minimum sol-to-gel transition temperatures (T_{gel}) could be precisely adjusted by changing the pH value of $FeCl_3$ in bicine solution, the molar ratio of Fe^{3+}/catechol ($R_{Fe/cat}$), and the concentration of iC-E-Ca^{2+} solution. The T_{gel} of the tested TCMBAs ranged from 28 to 42 °C, and further increase in temperature led to the

precipitation of TCMBAs. The optimized TCMBA formulation could be conveniently administered at room temperature and formed an instant seal (within 3–46 s) upon contact with body-temperature wounds. The iron-catechol coordination endowed TCMBAs with considerable cohesion and wet tissue adhesiveness (up to ~30 kPa), fast biodegradability (degraded in 6 days to one month), rapid shape-adaptability, favorable self-healing, as well as high elasticity (elongation up to ~1900 %). The intrinsic photothermal conversion ability, coupled with a thermo-induced antimicrobial effect achieved at ~48 °C, enabled mild photothermal therapy (PTT) against both pathogenic bacteria and cancer cells. TCMBAs exhibited a multifunctional 'attack-defense' property, combining proactive antimicrobial and antitumor actions ('attack') with protective barrier and tissue-regenerative functions ('defense'), making them suitable for treating complex wounds. Combined with NIR irradiation, the intrinsic antimicrobial activity of TCMBAs (derived from Fe^{3+} and citrate) synergistically promoted infected wound healing. Furthermore, in post-surgical cancerous wound models, the TCMBA + NIR combination therapy effectively inhibited tumor recurrence and metastasis while simultaneously promoting wound healing. This potent efficacy is attributed to a multi-mechanistic synergy: (i) Fe^{3+}-induced ferroptosis, (ii) the bidirectional regulation of citrate, which promotes apoptosis in tumor cells yet enhances the proliferation of normal skin cells, and (iii) the adjuvant effect of mild PTT. As a drug-free tissue adhesive, TCMBAs not only broaden the spectrum of available thermosensitive hydrogels but also establish a novel design paradigm for multifunctional therapeutic materials. This approach is expected to inspire further innovations in biomaterials development aimed at addressing complex challenges in regenerative medicine.

CRediT authorship contribution statement

Meimei Fu: Writing – review & editing, Writing – original draft, Visualization, Validation, Software, Resources, Project administration, Methodology, Investigation, Formal analysis, Data curation, Conceptualization. **Qiankun Shi:** Writing – review & editing, Writing – original draft, Visualization, Validation, Software, Resources, Project administration, Methodology, Investigation, Formal analysis, Data curation, Conceptualization. **Yitao Zhao:** Writing – review & editing, Writing – original draft, Visualization, Validation, Software, Resources, Project administration, Methodology, Investigation, Formal analysis, Data curation, Conceptualization. **Jintao Li:** Writing – review & editing, Methodology, Investigation, Data curation. **Zhuoyi Huang:** Writing – review & editing, Methodology, Investigation, Data curation. **Zhihui Lu:** Validation, Software, Resources. **Jian Yang:** Visualization, Supervision, Software, Resources, Funding acquisition. **Dongfang Zhou:** Writing – review & editing, Supervision, Resources, Funding acquisition, Conceptualization. **Jinshan Guo:** Writing – review & editing, Visualization, Validation, Software, Resources, Project administration, Funding acquisition, Conceptualization.

Ethics approval and consent to participate

All *in vivo* animal experimental procedures were conducted in accordance with Arrive's guidelines, performed with the approval of Guangdong Academy of Sciences (Approval No. 2021011), and performed according to the Animal Welfare Act and National Institute of Health (NIH) guidelines for the care and use of laboratory animals.

Declaration of competing interest

The authors declare that they have no known competing financial interests or personal relationships that could have appeared to influence the work reported in this paper.

Jian Yang is an editor-in-chief for Bioactive Materials and was not involved in the editorial review or the decision to publish this article. All authors declare that there are no competing interests.

Acknowledgements

This work was supported by the Natural Science Foundation of China (Grant No. 82272453, U21A2099 and 22275081), the National Key Research and Development Program of China (2024YFA1107800), the Guangdong Basic and Applied Basic Research Foundation (Grant No. 2024A1515012664), the Foundation of Muyuan Laboratory (Program ID: 13166022401), the Youth Talent of Guangdong Special Support Program (0620220207), and the Open Program from Guangdong Provincial Key Laboratory of Bone and Joint Degeneration Disease. Thanks to Qiaoying Huang for her help with the movie production.

Appendix A. Supplementary data

Supplementary data to this article can be found online at https://doi.org/10.1016/j.bioactmat.2026.01.010.

References

[1] G. Qiao, S. Li, X. Pan, P. Xie, R. Peng, X. Huang, M. He, J. Jiang, X. Chu, Surgical tumor–derived nanoplatform targets tumor-associated macrophage for personalized postsurgical cancer immunotherapy, Sci. Adv. 10 (13) (2024), https://doi.org/10.1126/sciadv.adk7955 eadk7955.

[2] T. Liang, Y. Dong, I. Cheng, P. Wen, F. Li, F. Liu, Q. Wu, E. Ren, P. Liu, H. Li, Z. Gu, In situ formation of biomolecular condensates as intracellular drug reservoirs for augmenting chemotherapy, Nat. Biomed. Eng. 8 (11) (2024) 1469–1482, https://doi.org/10.1038/s41551-024-01254-y.

[3] B. Guo, R. Dong, Y. Liang, M. Li, Haemostatic materials for wound healing applications, Nat. Rev. Chem 5 (11) (2021) 773–791, https://doi.org/10.1038/s41570-021-00323-z.

[4] Z. Chu, W. Zheng, W. Fu, J. Liang, W. Wang, L. Xu, X. Jiang, Z. Zha, H. Qian, Implanted microneedles loaded with sparfloxacin and zinc-manganese sulfide nanoparticles activates immunity for postoperative triple-negative breast cancer to prevent recurrence and metastasis, Adv. Sci. 12 (16) (2025) e2416270, https://doi.org/10.1002/advs.202416270.

[5] R. Lokwani, A. Josyula, T.B. Ngo, S. DeStefano, D. Fertil, M. Faust, K.M. Adusei, M. Bhuiyan, A. Lin, M. Karkanitsa, E. Maclean, P. Fathi, Y. Su, J. Liu, H. D. Vishwasrao, K. Sadtler, Pro-regenerative biomaterials recruit immunoregulatory dendritic cells after traumatic injury, Nat. Mater. 23 (1) (2024) 147–157, https://doi.org/10.1038/s41563-023-01689-9.

[6] Z. Lu, J. Zou, S. Li, M.J. Topper, Y. Tao, H. Zhang, X. Jiao, W. Xie, X. Kong, M. Vaz, H. Li, Y. Cai, L. Xia, P. Huang, K. Rodgers, B. Lee, J.B. Riemer, C.P. Day, R.C. Yen, Y. Cui, Y. Wang, Y. Wang, W. Zhang, H. Easwaran, A. Hulbert, K. Kim, R. A. Juergens, S.C. Yang, R.J. Battafarano, E.L. Bush, S.R. Broderick, S.M. Cattaneo, J.R. Brahmer, C.M. Rudin, J. Wrangle, Y. Mei, Y.J. Kim, B. Zhang, K.K. Wang, P. M. Forde, J.B. Margolick, B.D. Nelkin, C.A. Zahnow, D.M. Pardoll, F. Housseau, S. B. Baylin, L. Shen, M.V. Brock, Epigenetic therapy inhibits metastases by disrupting premetastatic niches, Nature 579 (7798) (2020) 284–290, https://doi.org/10.1038/s41586-020-2054-x.

[7] S. Turajlic, C. Swanton, Metastasis as an evolutionary process, Science 352 (6282) (2016) 169–175, https://doi.org/10.1126/science.aaf2784.

[8] Y. Wang, J. Yu, Z. Luo, Q. Shi, G. Liu, F. Wu, Z. Wang, Y. Huang, D. Zhou, Engineering endogenous tumor-associated macrophage-targeted biomimetic Nano-RBC to reprogram tumor immunosuppressive microenvironment for enhanced chemo-immunotherapy, Adv. Mater. 33 (39) (2021) e2103497, https://doi.org/10.1002/adma.202103497.

[9] S. Tohme, R.L. Simmons, A. Tsung, Surgery for cancer: a trigger for metastases, Cancer Res. 77 (7) (2017) 1548–1552, https://doi.org/10.1158/0008-5472.Can-16-1536.

[10] Z. Zhang, G. Kuang, S. Zong, S. Liu, H. Xiao, X. Chen, D. Zhou, Y. Huang, Sandwich-like Fibers/Sponge composite combining chemotherapy and hemostasis for efficient postoperative prevention of tumor recurrence and metastasis, Adv. Mater. 30 (49) (2018) e1803217, https://doi.org/10.1002/adma.201803217.

[11] H. Yuk, C.E. Varela, C.S. Nabzdyk, X. Mao, R.F. Padera, E.T. Roche, X. Zhao, Dry double-sided tape for adhesion of wet tissues and devices, Nature 575 (7781) (2019) 169–174, https://doi.org/10.1038/s41586-019-1710-5.

[12] J. Ding, J. Chen, L. Gao, Z. Jiang, Y. Zhang, M. Li, Q. Xiao, S.S. Lee, X. Chen, Engineered nanomedicines with enhanced tumor penetration, Nano Today 29 (2019) 100800, https://doi.org/10.1016/j.nantod.2019.100800.

[13] Z. Ma, G. Bao, J. Li, Multifaceted design and emerging applications of tissue adhesives, Adv. Mater. 33 (24) (2021) 2007663, https://doi.org/10.1002/adma.202007663.

[14] S. Nam, D. Mooney, Polymeric tissue adhesives, Chem. Rev. 121 (18) (2021) 11336–11384, https://doi.org/10.1021/acs.chemrev.0c00798.

[15] H. Ren, Z. Zhang, X. Cheng, Z. Zou, X. Chen, C. He, Injectable, self-healing hydrogel adhesives with firm tissue adhesion and on-demand biodegradation for sutureless wound closure, Sci. Adv. 9 (33) (2023), https://doi.org/10.1126/sciadv.adh4327 eadh4327.

[16] Y. Zhou, L. Yang, Z. Liu, Y. Sun, J. Huang, B. Liu, Q. Wang, L. Wang, Y. Miao, M. Xing, Z. Hu, Reversible adhesives with controlled wrinkling patterns for

programmable integration and discharging, Sci. Adv. 9 (15) (2023), https://doi.org/10.1126/sciadv.adf1043 eadf1043.
[17] K. Wu, M. Fu, Y. Zhao, E. Gerhard, Y. Li, J. Yang, J. Guo, Anti-oxidant anti-inflammatory and antibacterial tannin-crosslinked citrate-based mussel-inspired bioadhesives facilitate scarless wound healing, Bioact. Mater. 20 (2023) 93–110, https://doi.org/10.1016/j.bioactmat.2022.05.017.
[18] Y. Jeong, Y.K. Jo, B.J. Kim, B. Yang, K.I. Joo, H.J. Cha, Sprayable adhesive nanotherapeutics: mussel-protein-based nanoparticles for highly efficient locoregional cancer therapy, ACS Nano 12 (9) (2018) 8909–8919, https://doi.org/10.1021/acsnano.8b04533.
[19] S. Chen, Y. Luo, Y. He, M. Li, Y. Liu, X. Zhou, J. Hou, S. Zhou, In-situ-sprayed therapeutic hydrogel for oxygen-actuated Janus regulation of postsurgical tumor recurrence/metastasis and wound healing, Nat. Commun. 15 (1) (2024) 814, https://doi.org/10.1038/s41467-024-45072-x.
[20] C. Wang, W. Sun, Y. Ye, Q. Hu, H.N. Bomba, Z. Gu, In situ activation of platelets with checkpoint inhibitors for post-surgical cancer immunotherapy, Nat. Biomed. Eng. 1 (2) (2017) 11, https://doi.org/10.1038/s41551-016-0011.
[21] C. Wang, J. Wang, X. Zhang, S. Yu, D. Wen, Q. Hu, Y. Ye, H. Bomba, X. Hu, Z. Liu, G. Dotti, Z. Gu, In situ formed reactive oxygen species-responsive scaffold with gemcitabine and checkpoint inhibitor for combination therapy, Sci. Transl. Med. 10 (429) (2018), https://doi.org/10.1126/scitranslmed.aan3682 eaan3682.
[22] X. Lu, L. Miao, W. Gao, Z. Chen, K.J. McHugh, Y. Sun, Z. Tochka, S. Tomasic, K. Sadtler, A. Hyacinthe, Y. Huang, T. Graf, Q. Hu, M. Sarmadi, R. Langer, D. G. Anderson, A. Jaklenec, Engineered PLGA microparticles for long-term, pulsatile release of STING agonist for cancer immunotherapy, Sci. Transl. Med. 12 (556) (2020), https://doi.org/10.1126/scitranslmed.aaz6606 eaaz6606.
[23] S.O. Blacklow, J. Li, B.R. Freedman, M. Zeidi, C. Chen, D.J. Mooney, Bioinspired mechanically active adhesive dressings to accelerate wound closure, Sci. Adv. 5 (7) (2019), https://doi.org/10.1126/sciadv.aaw3963 eaaw3963.
[24] L. Xiao, P. Xie, J. Ma, K. Shi, Y. Dai, M. Pang, J. Luo, Z. Tan, Y. Ma, X. Wang, L. Rong, L. He, A bioinspired injectable, adhesive, and self-healing hydrogel with dual hybrid network for neural regeneration after Spinal cord injury, Adv. Mater. 35 (41) (2023) e2304896, https://doi.org/10.1002/adma.202304896.
[25] Y. Yang, Y. Liang, J. Chen, X. Duan, B. Guo, Mussel-inspired adhesive antioxidant antibacterial hemostatic composite hydrogel wound dressing via photo-polymerization for infected skin wound healing, Bioact. Mater. 8 (2022) 341–354, https://doi.org/10.1016/j.bioactmat.2021.06.014.
[26] W. Zhang, R. Wang, Z. Sun, X. Zhu, Q. Zhao, T. Zhang, A. Cholewinski, F.K. Yang, B. Zhao, R. Pinnaratip, P.K. Forooshani, B.P. Lee, Catechol-functionalized hydrogels: biomimetic design, adhesion mechanism, and biomedical applications, Chem. Soc. Rev. 49 (2) (2020) 433–464, https://doi.org/10.1039/c9cs00285e.
[27] C. Xie, X. Wang, H. He, Y. Ding, X. Lu, Mussel-inspired hydrogels for self-adhesive bioelectronics, Adv. Funct. Mater. 30 (25) (2020) 1909954, https://doi.org/10.1002/adfm.201909954.
[28] L. Wang, P. Chen, Y. Pan, Z. Wang, J. Xu, X. Wu, Q. Yang, M. Long, S. Liu, W. Huang, C. Ou, Y. Wu, Injectable photocurable Janus hydrogel delivering hiPSC cardiomyocyte-derived exosome for post-heart surgery adhesion reduction, Sci. Adv. 9 (31) (2023), https://doi.org/10.1126/sciadv.adh1753 eadh1753.
[29] X. Xu, X. Xia, K. Zhang, A. Rai, Z. Li, P. Zhao, K. Wei, L. Zou, B. Yang, W.K. Wong, P.W. Chiu, L. Bian, Bioadhesive hydrogels demonstrating pH-independent and ultrafast gelation promote gastric ulcer healing in pigs, Sci. Transl. Med. 12 (558) (2020), https://doi.org/10.1126/scitranslmed.aba8014 eaba8014.
[30] J. Guo, Z. Xie, R.T. Tran, D. Xie, D. Jin, X. Bai, J. Yang, Click chemistry plays a dual role in biodegradable polymer design, Adv. Mater. 26 (12) (2014) 1906–1911, https://doi.org/10.1002/adma.201305162.
[31] H. Wang, S. Huddleston, J. Yang, G.A. Ameer, Enabling proregenerative medical devices via citrate-based biomaterials: transitioning from inert to regenerative biomaterials, Adv. Mater. 36 (6) (2024) e2306326, https://doi.org/10.1002/adma.202306326.
[32] J. Guo, X. Tian, D. Xie, K. Rahn, E. Gerhard, M.L. Kuzma, D. Zhou, C. Dong, X. Bai, Z. Lu, J. Yang, Citrate-based tannin-bridged bone composites for lumbar fusion, Adv. Funct. Mater. 30 (27) (2020) 2002438, https://doi.org/10.1002/adfm.202002438.
[33] C. Ma, X. Tian, J.P. Kim, D. Xie, X. Ao, D. Shan, Q. Lin, M.R. Hudock, X. Bai, J. Yang, Citrate-based materials fuel human stem cells by metabonegenic regulation, Proc. Natl. Acad. Sci. USA 115 (50) (2018) E11741–e11750, https://doi.org/10.1073/pnas.1813000115.
[34] J. Guo, G.B. Kim, D. Shan, J.P. Kim, J. Hu, W. Wang, F.G. Hamad, G. Qian, E. B. Rizk, J. Yang, Click chemistry improved wet adhesion strength of mussel-inspired citrate-based antimicrobial bioadhesives, Biomaterials 112 (2017) 275–286, https://doi.org/10.1016/j.biomaterials.2016.10.010.
[35] X. Lu, S. Shi, H. Li, E. Gerhard, Z. Lu, X. Tan, W. Li, K.M. Rahn, D. Xie, G. Xu, F. Zou, X. Bai, J. Guo, J. Yang, Magnesium oxide-crosslinked low-swelling citrate-based mussel-inspired tissue adhesives, Biomaterials 232 (2020) 119719, https://doi.org/10.1016/j.biomaterials.2019.119719.
[36] M. Zhang, J. Liu, T. Zhu, H. Le, X. Wang, J. Guo, G. Liu, J. Ding, Functional macromolecular adhesives for bone fracture healing, ACS Appl. Mater. Interfaces 14 (1) (2022) 1–19, https://doi.org/10.1021/acsami.1c17434.
[37] M. Fu, Y. Zhao, Y. Wang, Y. Li, M. Wu, Q. Liu, Z. Hou, Z. Lu, K. Wu, J. Guo, On-Demand removable self-healing and pH-Responsive europium-releasing adhesive dressing enables inflammatory microenvironment modulation and angiogenesis for diabetic wound healing, Small 19 (3) (2023) e2205489, https://doi.org/10.1002/smll.202205489.
[38] Y. Zhao, X. Liu, F. Si, L. Huang, A. Gao, W. Lin, D.F. Hoft, Q. Shao, G. Peng, Citrate promotes excessive lipid biosynthesis and senescence in tumor cells for tumor therapy, Adv. Sci. 9 (1) (2022) e2101553, https://doi.org/10.1002/advs.202101553.
[39] I. Philippe, L. Hubert, The reduced concentration of citrate in cancer cells: an indicator of cancer aggressiveness and a possible therapeutic target, Drug Resist. Updates 29 (2016) 47–53, https://doi.org/10.1016/j.drup.2016.09.003.
[40] C. Zhang, B. Wu, Y. Zhou, F. Zhou, W. Liu, Z. Wang, Mussel-inspired hydrogels: from design principles to promising applications, Chem. Soc. Rev. 49 (11) (2020) 3605–3637, https://doi.org/10.1039/c9cs00849g.
[41] R. Liang, H. Yu, L. Wang, N. Wang, B.U. Amin, NIR light-triggered shape memory polymers based on mussel-inspired iron–catechol complexes, Adv. Funct. Mater. 31 (32) (2021) 2102621, https://doi.org/10.1002/adfm.202102621.
[42] M. Li, X. Sun, N. Zhang, W. Wang, Y. Yang, H. Jia, W. Liu, NIR-activated polydopamine-coated carrier-free "Nanobomb" for in situ On-Demand drug release, Adv. Sci. 5 (7) (2018) 1800155, https://doi.org/10.1002/advs.201800155.
[43] X. Li, J.F. Lovell, J. Yoon, X. Chen, Clinical development and potential of photothermal and photodynamic therapies for cancer, Nat. Rev. Clin. Oncol. 17 (11) (2020) 657–674, https://doi.org/10.1038/s41571-020-0410-2.
[44] H.S. Jung, P. Verwilst, A. Sharma, J. Shin, J.L. Sessler, J.S. Kim, Organic molecule-based photothermal agents: an expanding photothermal therapy universe, Chem. Soc. Rev. 47 (7) (2018) 2280–2297, https://doi.org/10.1039/c7cs00522a.
[45] X. Yuan, Y. Zhao, J. Li, X. Chen, Z. Lu, L. Li, J. Guo, Citrate-based mussel-inspired magnesium whitlockite composite adhesives augmented bone-to-tendon healing, J. Mater. Chem. B 9 (39) (2021) 8202–8210, https://doi.org/10.1039/d1tb01710a.
[46] L. Li, B. Yan, J. Yang, L. Chen, H. Zeng, Novel mussel-inspired injectable self-healing hydrogel with anti-biofouling property, Adv. Mater. 27 (7) (2015) 1294–1299, https://doi.org/10.1002/adma.201405166.
[47] L.C. Su, Z. Xie, Y. Zhang, K.T. Nguyen, J. Yang, Study on the antimicrobial properties of citrate-based biodegradable polymers, Front. Bioeng. Biotechnol. 2 (2014) 23, https://doi.org/10.3389/fbioe.2014.00023.
[48] L. Zhang, Y. Zhang, Y. Xue, Y. Wu, Q. Wang, L. Xue, Z. Su, C. Zhang, Transforming weakness into strength: photothermal-therapy-induced inflammation enhanced cytopharmaceutical chemotherapy as a combination anticancer treatment, Adv. Mater. 31 (5) (2019) 1805936, https://doi.org/10.1002/adma.201805936.
[49] Y. Liang, Z. Li, Y. Huang, R. Yu, B. Guo, Dual-dynamic-bond cross-linked antibacterial adhesive hydrogel sealants with On-Demand removability for post-wound-closure and infected wound healing, ACS Nano 15 (4) (2021) 7078–7093, https://doi.org/10.1021/acsnano.1c00204.
[50] C. Zhang, Y. Zhou, H. Han, H. Zheng, W. Xu, Z. Wang, Dopamine-triggered hydrogels with high transparency, Self-adhesion, and thermoresponse as skinlike sensors, ACS Nano 15 (1) (2021) 1785–1794, https://doi.org/10.1021/acsnano.0c09577.
[51] B. Shriky, A. Kelly, M. Isreb, M. Babenko, N. Mahmoudi, S. Rogers, O. Shebanova, T. Snow, T. Gough, Pluronic F127 thermosensitive injectable smart hydrogels for controlled drug delivery system development, Colloid Interface Sci. 565 (2020) 119–130, https://doi.org/10.1016/j.jcis.2019.12.096.
[52] X. Xu, X. Liu, L. Tan, Z. Cui, X. Yang, S. Zhu, Z. Li, X. Yuan, Y. Zheng, K.W. K. Yeung, P.K. Chu, S. Wu, Controlled-temperature photothermal and oxidative bacteria killing and acceleration of wound healing by polydopamine-assisted Au-hydroxyapatite nanorods, Acta Biomater. 77 (2018) 352–364, https://doi.org/10.1016/j.actbio.2018.07.030.
[53] M.C. Chen, K.W. Wang, D.H. Chen, M.H. Ling, C.Y. Liu, Remotely triggered release of small molecules from LaB6@SiO2-loaded polycaprolactone microneedles, Acta Biomater. 13 (2015) 344–353, https://doi.org/10.1016/j.actbio.2014.11.040.
[54] H. Li, T. Lv, H. Sun, G. Qian, N. Li, Y. Yao, T. Chen, Ultrastretchable and superior healable supercapacitors based on a double cross-linked hydrogel electrolyte, Nat. Commun. 10 (1) (2019) 536, https://doi.org/10.1038/s41467-019-08320-z.
[55] Y. Yang, W. Zhu, Z. Dong, Y. Chao, L. Xu, M. Chen, Z. Liu, 1D coordination polymer nanofibers for low-temperature photothermal therapy, Adv. Mater. 29 (40) (2017) 1703588, https://doi.org/10.1002/adma.201703588.
[56] A. Rajan, S.S. Laha, N.K. Sahu, N.D. Thorat, B. Shankar, Recent advancements and clinical aspects of engineered iron oxide nanoplatforms for magnetic hyperthermia-induced cancer therapy, Mater. Today Bio 29 (2024) 101348, https://doi.org/10.1016/j.mtbio.2024.101348.
[57] H. Lei, Z. Pei, C. Jiang, L. Cheng, Recent progress of metal-based nanomaterials with anti-tumor biological effects for enhanced cancer therapy, Explorations 3 (5) (2023) 20220001, https://doi.org/10.1002/exp.20220001.
[58] J. Drury, L.E.A. Young, T.L. Scott, C.O. Kelson, D. He, J. Liu, Y. Wu, C. Wang, H. L. Weiss, T. Fan, M.S. Gentry, R. Sun, Y.Y. Zaytseva, Tissue-specific downregulation of fatty acid synthase suppresses intestinal adenoma formation via coordinated reprograming of transcriptome and metabolism in the mouse model of apc-driven colorectal cancer, Int. J. Mol. Sci. 23 (12) (2022) 6510, https://doi.org/10.3390/ijms23126510.
[59] S. Singh, J. Dodt, P. Volkers, E. Hethershaw, H. Philippou, V. Ivaskevicius, D. Imhof, J. Oldenburg, A. Biswas, Structure functional insights into calcium binding during the activation of coagulation factor XIII A, Sci. Rep. 9 (1) (2019) 11324, https://doi.org/10.1038/s41598-019-47815-z.
[60] W. Han, B. Zhou, K. Yang, X. Xiong, S. Luan, Y. Wang, Z. Xu, P. Lei, Z. Luo, J. Gao, Y. Zhan, G. Chen, L. Liang, R. Wang, S. Li, H. Xu, Biofilm-inspired adhesive and antibacterial hydrogel with tough tissue integration performance for sealing hemostasis and wound healing, Bioact. Mater. 5 (4) (2020) 768–778, https://doi.org/10.1016/j.bioactmat.2020.05.008.
[61] W. Yang, X. Kang, X. Gao, Y. Zhuang, C. Fan, H. Shen, Y. Chen, J. Dai, Biomimetic natural biopolymer-based wet-tissue adhesive for tough adhesion, seamless sealed, Emergency/Nonpressing hemostasis, and promoted wound healing, Adv. Funct. Mater. 33 (6) (2023) 2211340, https://doi.org/10.1002/adfm.202211340.

[62] M. Fu, Q. Xiang, Z. Huang, W. Luo, Z. Fang, J. Li, Y. Li, Z. Xia, Y. Huang, Y. Zhao, W. Liao, J. Guo, Photo-cross-linked and photothermal Flammulina velutipes polysaccharide hydrogel loaded with caffeic acid-copper nanozyme for diabetic wound healing, ACS Appl. Mater. Interfaces 17 (38) (2025) 53145–53167, https://doi.org/10.1021/acsami.5c11453.
[63] Z. Arabpour, F. Abedi, M. Salehi, S.M. Baharnoori, M. Soleimani, A.R. Djalilian, Hydrogel-based skin regeneration, Int. J. Mol. Sci. 25 (4) (2024) 1982, https://doi.org/10.3390/ijms25041982.
[64] H. Xu, S. Yan, E. Gerhard, D. Xie, X. Liu, B. Zhang, D. Shi, G.A. Ameer, J. Yang, Citric acid: a nexus between cellular mechanisms and biomaterial innovations, Adv. Mater. 36 (32) (2024) 2402871, https://doi.org/10.1002/adma.202402871.
[65] Y. Wang, Y. Zhang, Y.P. Yang, M.Y. Jin, S. Huang, Z.M. Zhuang, T. Zhang, L.L. Cao, X.Y. Lin, J. Chen, Y.Z. Du, J. Chen, W.Q. Tan, Versatile dopamine-functionalized hyaluronic acid-recombinant human collagen hydrogel promoting diabetic wound healing via inflammation control and vascularization tissue regeneration, Bioact. Mater. 35 (2024) 330–345, https://doi.org/10.1016/j.bioactmat.2024.02.010.
[66] J.A. Wright, T. Richards, S.K. Srai, The role of iron in the skin and cutaneous wound healing, Front. Pharmacol. 5 (2014) 156, https://doi.org/10.3389/fphar.2014.00156.
[67] T. Ma, X. Zhai, Y. Huang, M. Zhang, X. Zhao, Y. Du, C. Yan, A smart nanoplatform with photothermal antibacterial capability and antioxidant activity for chronic wound healing, Adv. Healthcare Mater. 10 (13) (2021) e2100033, https://doi.org/10.1002/adhm.202100033.
[68] L. He, D. Di, X. Chu, X. Liu, Z. Wang, J. Lu, S. Wang, Q. Zhao, Photothermal antibacterial materials to promote wound healing, J. Contr. Release 363 (2023) 180–200, https://doi.org/10.1016/j.jconrel.2023.09.035.
[69] Z. Chu, T. Tian, Z. Tao, J. Yang, B. Chen, H. Chen, W. Wang, P. Yin, X. Xia, H. Wang, H. Qian, Upconversion nanoparticles@AgBiS(2) core-shell nanoparticles with cancer-cell-specific cytotoxicity for combined photothermal and photodynamic therapy of cancers, Bioact. Mater. 17 (2022) 71–80, https://doi.org/10.1016/j.bioactmat.2022.01.010.
[70] C. Xue, M. Li, C. Liu, Y. Li, Y. Fei, Y. Hu, K. Cai, Y. Zhao, Z. Luo, NIR-actuated remote activation of ferroptosis in target tumor cells through a photothermally responsive iron-chelated biopolymer nanoplatform, Angew. Chem. Int. Ed. 60 (16) (2021) 8938–8947, https://doi.org/10.1002/anie.202016872.
[71] Z. Lin, J. Ling, A.M. Omer, X.K. Ouyang, L. Mei, N. Wang, Flexible microneedle platform for synergistic Chemo/Photothermal ferroptosis therapy via P-Glycoprotein inhibition in breast cancer, ACS Appl. Mater. Interfaces 17 (30) (2025) 42807–42823, https://doi.org/10.1021/acsami.5c09308.
[72] L. Jing, W. Xiao, Z. Hu, X. Liu, M. Yuan, A systematic review of nanoparticle-mediated ferroptosis in Glioma therapy, Int. J. Nanomed. 20 (2025) 5779–5797, https://doi.org/10.2147/ijn.S523008.
[73] W. Zhang, X. Wang, P. Wang, Q. Li, Y. Zhang, X. Meng, G. Tian, J. Xiao, G. Zhang, Glucose transporter protein 1-targeted polymetallic coordination nanopolymer remodeled cisplatin-resistant microenvironment for enhanced chemotherapy of lung cancer, J. Colloid Interface Sci. 700 (Pt 2) (2025) 138424, https://doi.org/10.1016/j.jcis.2025.138424.
[74] M.J. Rao, H. Zuo, Q. Xu, Genomic insights into citrus domestication and its important agronomic traits, Plant Commun. 2 (1) (2021) 100138, https://doi.org/10.1016/j.xplc.2020.100138.
[75] P. Icard, A. Coquerel, Z. Wu, J. Gligorov, D. Fuks, L. Fournel, H. Lincet, L. Simula, Understanding the central role of citrate in the metabolism of cancer cells and tumors: an update, Int. J. Mol. Sci. 22 (12) (2021) 6587, https://doi.org/10.3390/ijms22126587.
[76] J. Wu, N. Liu, J. Chen, Q. Tao, Q. Li, J. Li, X. Chen, C. Peng, The tricarboxylic acid cycle metabolites for cancer: friend or enemy, Research 7 (2024) 351, https://doi.org/10.34133/research.0351.
[77] J.G. Ren, P. Seth, H. Ye, K. Guo, J.I. Hanai, Z. Husain, V.P. Sukhatme, Citrate suppresses tumor growth in multiple models through inhibition of glycolysis, the tricarboxylic acid cycle and the IGF-1R pathway, Sci. Rep. 7 (1) (2017) 4537, https://doi.org/10.1038/s41598-017-04626-4.
[78] W. Wang, Y. Gao, W. Xu, Y. Xu, N. Zhou, Y. Li, M. Zhang, B.Z. Tang, The one-stop integrated nanoagent based on photothermal therapy for deep infection healing and inflammation inhibition, Adv. Mater. 36 (3) (2024) e2307785, https://doi.org/10.1002/adma.202307785.
[79] X. Qi, E. Cai, Y. Xiang, C. Zhang, X. Ge, J. Wang, Y. Lan, H. Xu, R. Hu, J. Shen, An immunomodulatory hydrogel by hyperthermia-assisted self-cascade glucose depletion and ROS scavenging for diabetic foot ulcer wound therapeutics, Adv. Mater. 35 (48) (2023) e2306632, https://doi.org/10.1002/adma.202306632.
[80] Y. Li, Y. Miao, L. Yang, Y. Zhao, K. Wu, Z. Lu, Z. Hu, J. Guo, Recent advances in the development and antimicrobial applications of metal-phenolic networks, Adv. Sci. 9 (27) (2022) e2202684, https://doi.org/10.1002/advs.202202684.
[81] Y. Li, G. Zheng, Y. Lu, J. Liu, F. Qin, Q. Zhou, L. He, X. Mao, Staged low-frequency ultrasound synergized with composite hydrogel to achieve "Rapid Antimicrobial-Ordered Regeneration" of infected wounds, Adv. Healthcare Mater. (2025) e03471, https://doi.org/10.1002/adhm.202503471.
[82] C. Zhang, X. Zhang, F. Li, B. Li, M. Zhang, W. Li, P. Zhuge, J. Yao, Y. Zhang, S. Chen, Y. Fang, C. Cai, Thermosensitive hydrogel integrated with bimetallic nano-enzymes for modulating the microenvironment in diabetic wound beds, Adv. Sci. 12 (6) (2025) e2411575, https://doi.org/10.1002/advs.202411575.
[83] C. Yang, X. Liao, K. Zhou, Y. Yao, X. He, W. Zhong, D. Zheng, Y. Yang, M. Li, M. Zhou, Y. Zhou, L. Li, Y. Bai, K. Shi, Z. Qian, Multifunctional nanoparticles and collagenase dual loaded thermosensitive hydrogel system for enhanced tumor-penetration, reversed immune suppression and photodynamic-immunotherapy, Bioact. Mater. 48 (2025) 1–17, https://doi.org/10.1016/j.bioactmat.2025.02.014.
[84] C. Lian, J. Liu, W. Wei, X. Wu, T. Goto, H. Li, R. Tu, H. Dai, Mg-gallate metal-organic framework-based sprayable hydrogel for continuously regulating oxidative stress microenvironment and promoting neurovascular network reconstruction in diabetic wounds, Bioact. Mater. 38 (2024) 181–194, https://doi.org/10.1016/j.bioactmat.2024.04.028.
[85] M. Derakhshan-Sefidi, Y. Azarakhsh, Dual biomedical applications of Quaternary ammonium salts: antimicrobial and anticancer perspectives, Micro Nano Bio Aspects 4 (3) (2025) 54–64, https://doi.org/10.22034/mnba.2025.544530.1157.
[86] M. Teng, L. Zhang, Y. Fan, M. Fu, Z. Li, Microneedles loaded with PD-L1 inhibitor and doxorubicin GelMA hydrogel for melanoma immunochemotherapy, Mater. Des. 255 (2025) 114238, https://doi.org/10.1016/j.matdes.2025.114238.
[87] Z. Chu, H. Chen, P. Wang, W. Wang, J. Yang, J. Sun, B. Chen, T. Tian, Z. Zha, H. Wang, H. Qian, Phototherapy using a fluoroquinolone antibiotic drug to suppress tumor migration and proliferation and to enhance apoptosis, ACS Nano 16 (3) (2022) 4917–4929, https://doi.org/10.1021/acsnano.2c00854.